

Quenching of Satellite Galaxies at the Outskirts of Galaxy Clusters

Elad Zinger^{1*}, Avishai Dekel¹, Andrey V. Kravtsov² & Daisuke Nagai³

¹*Center for Astrophysics and Planetary Science, Racah Institute of Physics, The Hebrew University, Jerusalem 91904, Israel*

²*Department of Astronomy & Astrophysics, The University of Chicago, Chicago, IL 60637 USA*

³*Department of Physics, Yale University, New Haven, CT 06520, USA*

Submitted to MNRAS 8 October 2016

ABSTRACT

We find, using cosmological simulations of galaxy clusters, that the hot X-ray emitting intra-cluster medium (ICM) enclosed within the outer accretion shock extends out to $R_{\text{shock}} \sim (2-3)R_{\text{vir}}$, where R_{vir} is the standard virial radius of the halo. Using a simple analytic model for satellite galaxies in the cluster, we evaluate the effect of ram-pressure stripping on the gas in the inner discs and in the haloes at different distances from the cluster centre. We find that significant removal of star-forming disc gas occurs only at $r \lesssim 0.5R_{\text{vir}}$, while gas removal from the satellite halo is also efficient between R_{vir} and R_{shock} . This leads to quenching of star formation by starvation over 2–3 Gyr, prior to the satellite entry to the inner cluster halo. This can explain the presence of quenched galaxies, preferentially discs, at the outskirts of galaxy clusters, and the delayed quenching of satellites compared to central galaxies.

Key words: galaxies: clusters: general – galaxies: clusters: intracluster medium – galaxies: star formation – galaxies: evolution

1 INTRODUCTION

The link between the properties of galaxies and their environment has long been known, and nowhere is this link clearer than in galaxy clusters. Galaxies which reside in groups and clusters are more likely to be ‘quenched’, i.e. characterized by quiescent star formation, and possess less atomic and molecular gas than similar ‘field’ galaxies (Oemler 1974; Butcher & Oemler 1978; Dressler 1980).

In recent years, numerous observations have established that the galaxy–environment relation in galaxy clusters extends farther than previously assumed, out to $\sim (2-3)R_{\text{vir}}$. In particular, an elevated fraction of quenched galaxies was detected beyond the virial radius of the clusters compared with similar populations of ‘field’ galaxies (Balogh et al. 2000; Solanes et al. 2002; Verdugo et al. 2008; Braglia et al. 2009; Hansen et al. 2009; Park & Hwang 2009; von der Linden et al. 2010; Wetzel et al. 2012 and see Boselli & Gavazzi 2006 for an extensive review). Of particular interest is the phenomenon of ‘galactic conformity’ (Weinmann et al. 2006; Ann et al. 2008; Kauffmann et al. 2010) which finds a positive correlation between the star formation of central galaxies and their satellites, even for satellites found beyond the virial radius of the host halo.

One possible explanation for the extended effect of the environment is that the quenched, gas-poor galaxies observed are ‘pre-processed’ galaxies which were already subjected to quenching mechanisms in smaller haloes prior to becoming satellites in the cluster (Mihos 2004; Fujita 2004). Another explanation is that these are actually ‘ejected’ or ‘splashback’ galaxies, i.e. galaxies which entered the virial radius on a highly eccentric orbit at a much earlier time, passed through the central regions of the cluster and are now found beyond the virial radius once again (Mamon et al. 2004; Gill et al. 2005). In their passage through the inner regions of the cluster myriad processes such as tidal stripping (Zwicky 1951) ram-pressure stripping (Gunn & Gott 1972), thermal evaporation (Cowie & Songaila 1977), and encounters with other satellites (‘harassment’) (Moore et al. 1996, 1999) can lead to gas depletion and star formation quenching (Mamon et al. 2004; Wetzel et al. 2014). However, some studies have indicated that a substantial fraction are infalling into the system for the first time (Cen 2014; Fang et al. 2016). Bahé et al. (2013) in their analysis of satellites in simulated clusters find that neither of these explanations is sufficient to account for the quenched fraction at the cluster outskirts.

Another, more obvious explanation is that the cluster environment actually extends to beyond the virial radius, contrary to what is commonly assumed. It is well established that an accretion shock forms around the nodes of

* E-mail: elad.zinger@mail.huji.ac.il

the cosmic web where a convergence of mass accretion takes place (Bertschinger 1985; Furlanetto & Loeb 2004; Keres et al. 2005). The virial accretion shock, though unstable in low mass haloes, is a robust feature in massive haloes of $> 10^{12} M_{\odot}$ (Birnboim & Dekel 2003; Dekel & Birnboim 2006), and found consistently in numerical simulations (e.g. Keshet et al. 2003). Analytic studies (Voit et al. 2003; Book & Benson 2010) have shown that in cluster sized systems, the virial shock should be found at $\sim 1.5R_{\text{vir}}$, and, as we show below, numerical simulations have also found that in clusters the virial shock extends much farther than the virial radius (Molnar et al. 2009; Lau et al. 2015).

Galaxies crossing the accretion shock, which is found at $\sim (2-3)R_{\text{vir}}$, enter the ‘Intra-Cluster Medium’ (ICM) – gas which has been shock heated to 10^7-10^8 K and is in near hydro-static equilibrium within the potential well of the dark matter halo, radiating primarily in the X-ray (Sarazin 1988). Within the ICM the satellites are subjected to the aforementioned environmental processes which can lead to gas depletion and star-formation quenching.

In this study we focus on the effect of gas removal from the galaxy due to the ram-pressure exerted by the ICM as a result of the relative motion of galaxy in the medium. This process is commonly called ram-pressure stripping (hereafter RPS). The effects of RPS on galaxies close to the centres of clusters has been studied since the pioneering work of Gunn & Gott (1972) who derived an estimate for the effect (see also Gisler 1976). Direct evidence of RPS in action can be found in detailed analyses of specific galaxies (Boselli et al. 2006; Abramson et al. 2011; Ehlert et al. 2013; Ebeling et al. 2014; Abramson & Kenney 2014; Kenney et al. 2014), while large observational surveys of cluster satellites, coupled with analytic galaxy evolution models reveal its role in determining satellite properties (Cayatte et al. 1994; Boselli et al. 2009; Scott et al. 2010). The issue has also been explored numerically in idealized, ‘wind tunnel’ simulations (Gisler 1976; Balsara et al. 1994; Quilis et al. 2000; Tonnesen & Bryan 2009; Weinberg 2014), simple systems (Roediger & Brüggen 2007; Kapferer et al. 2008, 2009) and in cosmological settings (Tonnesen et al. 2007; Vollmer et al. 2001). See also Roediger (2009) for an extensive review. The insights from analytic and numerical studies have also been applied in semi-analytic modeling of cluster systems (Font et al. 2008; Book & Benson 2010).

A galactic system, consisting of a galaxy surrounded by a gas halo embedded in a dark matter halo, undergoing RPS will first shed the hot gas in the halo before the gas within the galaxy is affected (Larson et al. 1980; McCarthy et al. 2008; Bekki 2009; Bahé et al. 2013). In regions of intermediate densities, the ram-pressure may remove the gas halo, but not the gas from the galaxy, eventually leading to star formation quenching by ‘starvation’, once the star-forming gas inside the galaxy is passively consumed by star formation or removed by feedback-driven outflows (Kawata & Mulchaey 2008). As stars are formed, the dwindling gas reservoir within the galaxy can no longer be replenished from the halo, and the galaxy is quenched, albeit over longer time-scales.

In this paper we demonstrate, through the use of a suite of zoom-in simulations of galaxy clusters, that the zone of the cluster influence on star-formation quenching, i.e. the virial accretion shock, extends well beyond the standard

Cluster	M_{vir} ($10^{14} M_{\odot}$)	R_{vir} (Mpc)	T_{vir} (10^7 K)	V_{vir} (km s^{-1})
CL101	22.1	3.37	10.1	1678
CL102	13.7	2.88	7.4	1433
CL103	15.7	3.01	8.1	1497
CL104	11.9	2.74	6.7	1365
CL105	12.0	2.75	6.7	1369
CL106	9.5	2.54	5.8	1266
CL107	6.6	2.26	4.5	1125
CL3	6.3	2.22	4.4	1107
CL5	3.1	1.76	2.8	875
CL6	3.3	1.80	2.9	894
CL7	3.3	1.78	2.8	886
CL9	1.9	1.48	1.7	739
CL10	1.3	1.32	1.6	658
CL11	1.8	1.45	1.9	721
CL14	1.7	1.43	1.8	709
CL24	0.86	1.14	1.2	569

Table 1. Cluster Properties at $z = 0$. Virial quantities were calculated for an overdensity of $\Delta_{\text{vir}} = 337$ above the mean density of the universe.

Cluster	M_{vir} ($10^{14} M_{\odot}$)	R_{vir} (Mpc)	T_{vir} (10^7 K)	V_{vir} (km s^{-1})
CL101	3.3	1.29	4.0	1053
CL102	3.3	1.28	4.0	1051
CL103	2.9	1.23	3.7	1009
CL104	7.2	1.66	6.7	1362
CL105	6.2	1.58	6.0	1296
CL106	2.6	1.18	3.3	965
CL107	2.9	1.22	3.6	1002
CL3	2.8	1.21	3.6	995
CL5	1.8	1.04	2.6	858
CL6	2.4	1.15	3.2	946
CL7	2.3	1.13	3.1	929
CL9	1.2	0.91	2.0	744
CL10	1.1	0.89	1.9	730
CL11	0.86	0.78	1.5	643
CL14	0.99	0.86	1.8	703
CL24	0.37	0.62	0.9	505

Table 2. Cluster Properties at $z = 0.6$. Virial quantities were calculated for an overdensity of $\Delta_{\text{vir}} = 224$ above the mean density of the universe.

virial radius derived from the density contrast. We explore, via simple analytic models, the effect of RPS on the gas haloes surrounding galaxies and on the gas within the galaxies themselves, at different radii in the host cluster and in its outskirts, in an attempt to ascertain the main quenching channel responsible for the quenched galaxy population found beyond the virial radius.

The paper is organized as follows: in §2, we describe the suite of simulated clusters and in §3 we determine the location of the virial accretion shock. We construct analytic models to study the effectiveness of RPS on the halo gas of satellites in §4 and do the same for RPS of gas from the galactic discs in §5. In §6, we explore the implications of RPS on star formation quenching. In §7, we discuss the strengths and weaknesses of our RPS models and in §8 we summarize our findings.

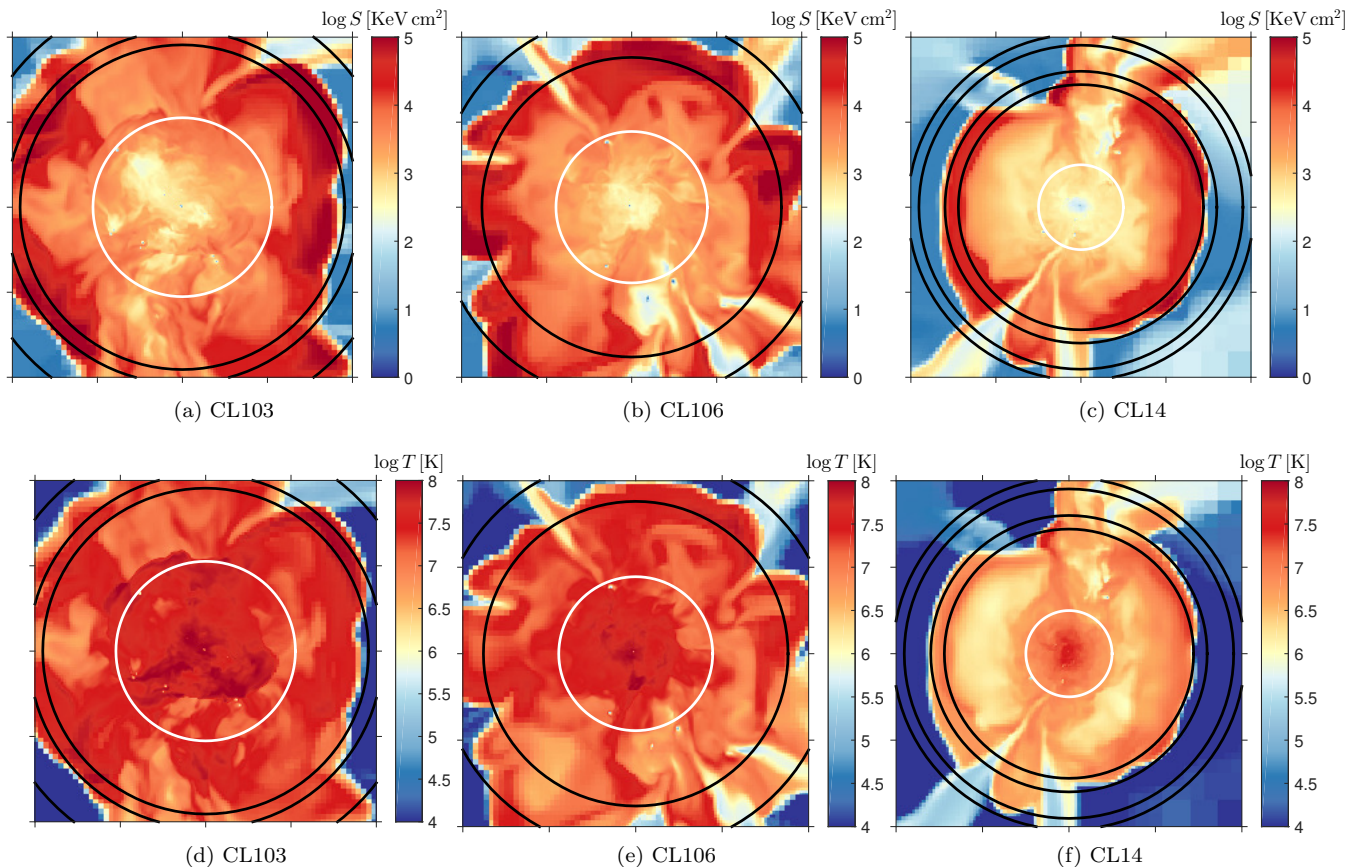


Figure 1. Entropy and temperature maps (top and bottom, respectively) of 3 representative clusters at $z = 0$ are plotted in box of size $8 \text{ Mpc } h^{-1}$ (see Table 1 for details). The shock front can be seen to extend well beyond the virial radius which is marked by the white circles. The entropy is low in the centre of the cluster and rises to a peak near the shock front, before dropping sharply, allowing a simple method of identifying the shock front. Black circles mark these drops in the entropy profile (see §3.2). The temperature is highest in the centre of the cluster and drops gradually outwards, with a sharp drop in temperature seen at the shock front. The complex shape of the shock front is evident. Lower entropy gas streams flowing towards the centre can also be seen.

2 SIMULATIONS

The simulation suite analysed in this study is comprised of 16 cluster-sized systems at $z = 0$ spanning a mass range of $8.6 \times 10^{13} - 2.2 \times 10^{15} M_{\odot}$, and their most massive progenitors at $z = 0.6$. The systems were extracted from cosmological simulations in a flat Λ CDM model: $\Omega_m = 1 - \Omega_{\Lambda} = 0.3$, $\Omega_b = 0.04286$, $h = 0.7$, and $\sigma_8 = 0.9$, where the Hubble constant is defined as $100h \text{ km s}^{-1} \text{ Mpc}^{-1}$, and σ_8 is the power spectrum normalization on an $8h^{-1} \text{ Mpc}$ scale. The simulations were carried out with the Adaptive Refinement Tree (ART) N -body +gas-dynamics code (Kravtsov 1999), an Eulerian code that uses adaptive refinement in space and time, and (non-adaptive) refinement in mass (Klypin et al. 2001) to reach the high dynamic range required to resolve cores of haloes formed in self-consistent cosmological simulations.

The computational boxes of the large-scale cosmological simulations were $120h^{-1} \text{ Mpc}$ and $80h^{-1} \text{ Mpc}$, and the simulation grid was adaptively refined to achieve a peak spatial resolution of order ~ 7 and $5h^{-1} \text{ kpc}$ respectively. These simulations are discussed in detail in Kravtsov et al. (2006), Nagai et al. (2007b) and Nagai et al. (2007a). The adaptive mesh refinement technique employed in the simulation is especially suited to capture discontinuous features such

as shock waves and contact discontinuities which make it especially suitable for our purposes.

Besides the basic dynamical processes of collisionless matter (dark matter and stars) and gas-dynamics, several physical processes critical for galaxy formation are incorporated: star formation, metal enrichment and feedback due to Type II and Type Ia supernovae, and self-consistent advection of metals. The cooling and heating rates take into account Compton heating and cooling of plasma, UV heating (Haardt & Madau 1996), and atomic and molecular cooling, which is tabulated for the temperature range $10^2 < T < 10^9 \text{ K}$, a grid of metallicities, and UV intensities using the CLOUDY code (version 96b4, Ferland et al. 1998). The CLOUDY cooling and heating rates take into account metallicity of the gas, which is calculated self-consistently in the simulation, so that the local cooling rates depend on the local metallicity of the gas. The star formation recipe incorporated in these simulations is observationally motivated (e.g. Kennicutt 1998) and the code also accounts for the stellar feedback on the surrounding gas, including injection of energy and heavy elements (metals) via stellar winds, supernovae, and secular mass loss. The simulations do not include an AGN feedback process.

The main purpose of this paper is to investigate the

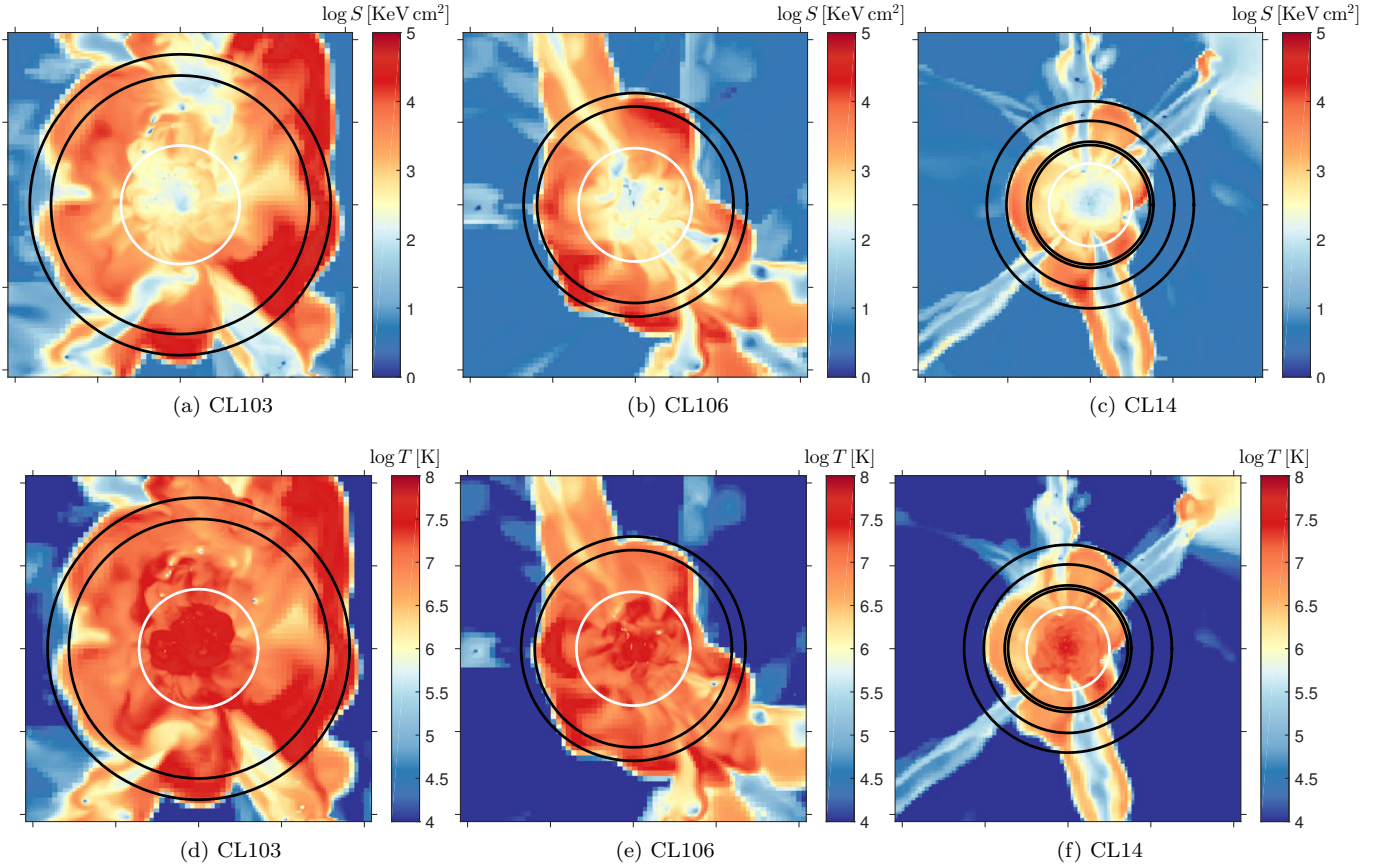


Figure 2. Entropy and temperature maps (top and bottom, respectively) of the 3 representative clusters at $z = 0.6$ are shown in a box of size 5 Mpc h^{-1} (see Table 2 for details). The cluster dimension and radii are shown in proper coordinates. As before, black circles drops in the entropy profile which we use to identify the locations of the shock fronts. At this redshift the shock front already extends well beyond the virial radius. The intricate shape of the shock front is due in part to the large scale filaments that ‘puncture’ the shock front which expands in lobes between the streams. Shocks can already be seen surrounding the large scale filaments feeding the cluster (b) & (c), merging seamlessly with the virial shock front.

effect of the environment at the cluster outskirts on the satellite galaxies within the cluster, focusing on mass-loss mechanism and the quenching of star formation. The resolution of the simulations is not high enough to properly model the galaxies within the cluster since the peak resolution is of order the scale radius of a typical disc galaxy. Instead we construct analytic models of the galaxies with which to examine the effects of the environment.

The virial parameters M_{vir} and R_{vir} are defined by the relation

$$\frac{3M_{\text{vir}}}{4\pi R_{\text{vir}}^3} = \Delta_{\text{vir}} \rho_{\text{ref}}, \quad (1)$$

with various choices in the literature for the overdensity parameter ($\Delta_{\text{vir}} = 178, 200, 337$) and reference density ρ_{ref} – either ρ_{crit} or $\rho_{\text{mean}} = \rho_{\text{crit}} \Omega_m$. Additional distance scales for clusters are sometimes set by overdensity factors of 500 and 1500.

In this paper, the virial quantities of the mass, radius, velocity and temperature ($M_{\text{vir}}, R_{\text{vir}}, V_{\text{vir}}, T_{\text{vir}}$) of the clusters are defined for an overdensity $\Delta_{\text{vir}} = 337$ at $z = 0$ and $\Delta_{\text{vir}} = 224$ at $z = 0.6$ above ρ_{mean} , the mean density of the universe (Bryan & Norman 1998). The properties of the

clusters for $z = 0$ and $z = 0.6$ are summarized in Tables 1 and 2 respectively.

3 VIRIAL SHOCK VERSUS VIRIAL RADIUS

3.1 Cluster Maps

We examine our cluster systems at $z = 0.6$ and $z = 0$ and find that the accretion shock extends well beyond the virial radius in all cases. This can be seen in entropy and temperature maps of a representative sample of clusters (CL103, CL106, CL14) at $z = 0$ in Fig. 1, where the entropy is defined as $S \propto T \rho^{-2/3}$. Furthermore, examining the same systems at $z = 0.6$ in Fig. 2 shows that this is the case at that redshift as well.

Detailed examination of the virial shock in the maps shows it to be spherical only in the roughest approximation and that in reality it contains many features and extends to different extents in different directions. The shock front is sometimes segmented into ‘lobes’ (e.g. Figs. 1b and 2c), by the large scale filaments which pierce the shock front (e.g. Fig. 1c). In some cases it can be seen to merge seamlessly

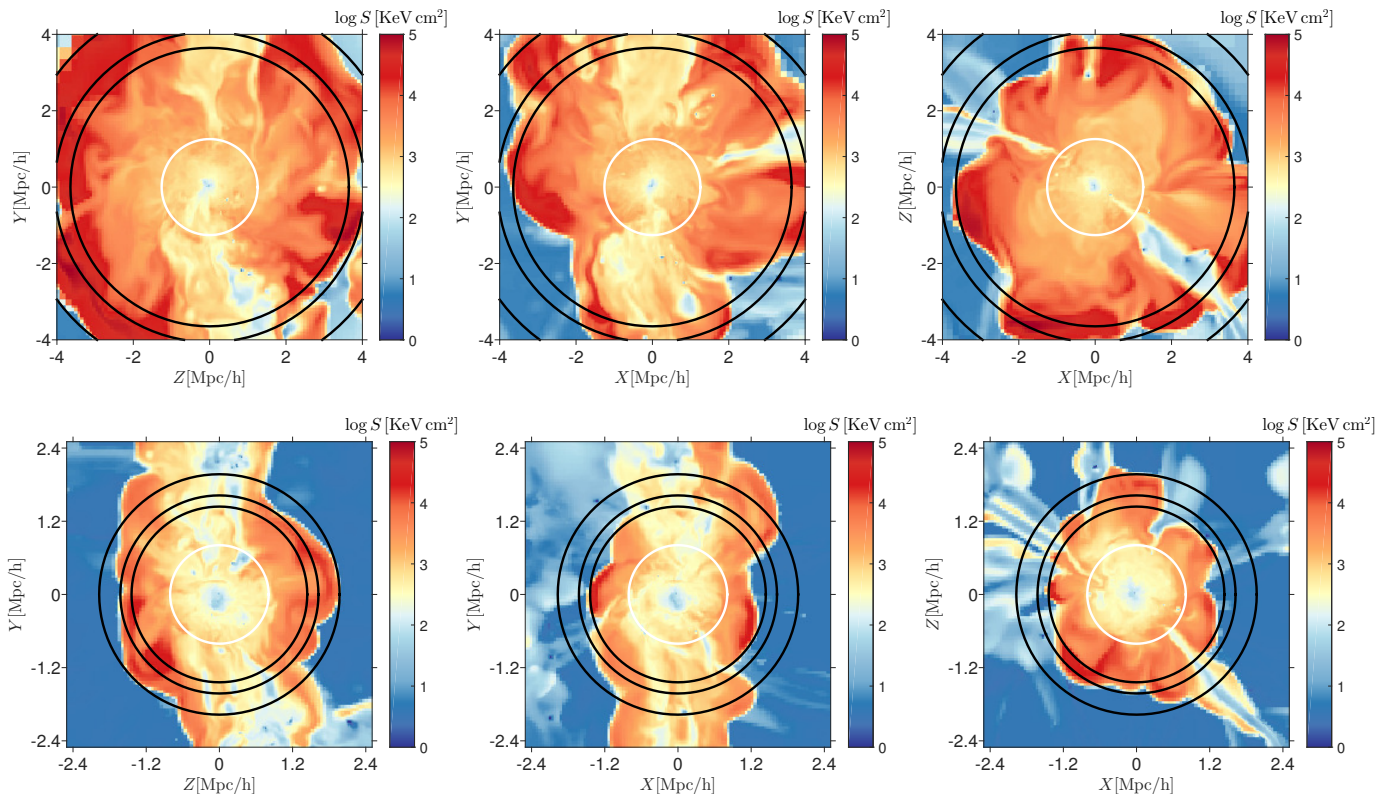


Figure 3. Entropy maps of the cluster CL6 in three orthogonal projections at $z = 0.0$ (top) and $z = 0.6$ (bottom). White circles mark the virial radius and black circles mark the approximate cluster edge as defined in §3.2. We see that even if an edge estimation does not seem to apply in a given projection, it corresponds to a shock front best observed from a different projection, due to the irregular topography of the shock front.

with the virial shock surrounding the large scale filaments (e.g. Figs. 2a and 2c).

The black circles in Figs. 1 and 2 mark the approximate positions of the accretion shock which we estimate using the entropy profile in the next section (§3.2). At first glance, some of the estimations may seem erroneous since they do not appear to correspond to the shock position in a given projection, when in fact they are indicative of the shock position better viewed from a different direction. This can be most clearly seen in Fig. 3.

In Fig. 3 we map cluster CL6 from 3 different projections. The virial shock can be seen to extend out to different distances in each direction though in all cases it is found well beyond the virial radius. In this particular system, the cluster can be seen to be positioned along a cosmic web filament of stretching in the Y direction. As can be seen, there is a cylindrical virial shock around the filament as well (this is most evident in the $z = 0.6$ maps, top), which merges seamlessly with the more spherical virial shock of the cluster. This is expected for massive filaments, of longitudinal density higher than $10^{12} M_{\odot}/\text{Mpc}$, which feed massive clusters at low redshifts, as shown by Birnboim et al. (2016).

In this cluster, and in most other systems as well, the lower entropy filaments can be seen to penetrate deep into the cluster virial shock, as far as the virial radius and even, in some cases, into the very central regions of the cluster. In Zinger et al. (2016) we address the issue of these gas streams, their origin and structure as well as the way they

carry in energy which heats and stirs up turbulence in the inner regions of the ICM.

3.2 Determining the Shock Edge

As can be seen in the temperature and entropy maps of the clusters (Figs. 1 to 3), the edge of the virial shock is characterized by a sharp drop in temperature and entropy of several orders of magnitude. Within the shock, the temperature rises gradually towards the centre of the cluster, whereas the entropy in the cluster drops, such that the entropy achieves its peak value close to the shock front.

Spherically averaged entropy and temperature profiles were created for all the cluster systems at both epochs, several representative cases of which are shown in Figs. 4 and 5. These profiles are in general agreement with observations (Simionescu et al. 2013) beyond the central regions of the cluster ($r > 0.05 R_{\text{vir}}$).

The temperature profiles show that the virial shock, characterized by a steep jump in temperature, is found at $\gtrsim 2 R_{\text{vir}}$. The reason the jump in temperature is not as large nor as sharp as in the maps is due to the fact that the profile is averaged over a spherical shell and as we have seen, the shock front is not spherical, leading to a smearing of the shock front signature. Behind the shock front, as one moves towards the centre, the temperature rises steadily reaching the virial temperature value at $\sim (0.3-0.4) R_{\text{vir}}$. The constant rise makes the identification of the shock front some-

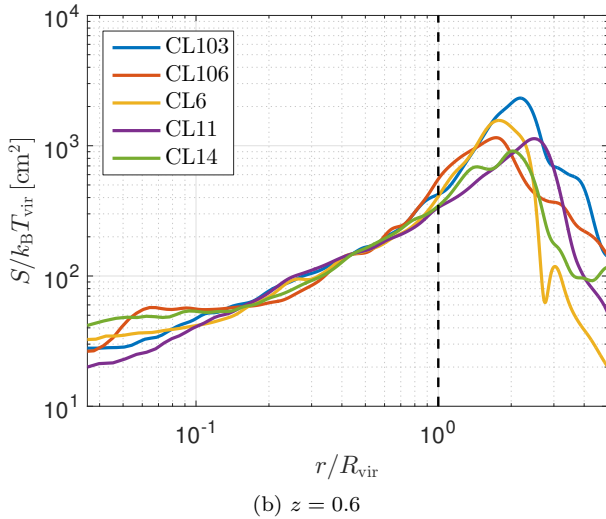
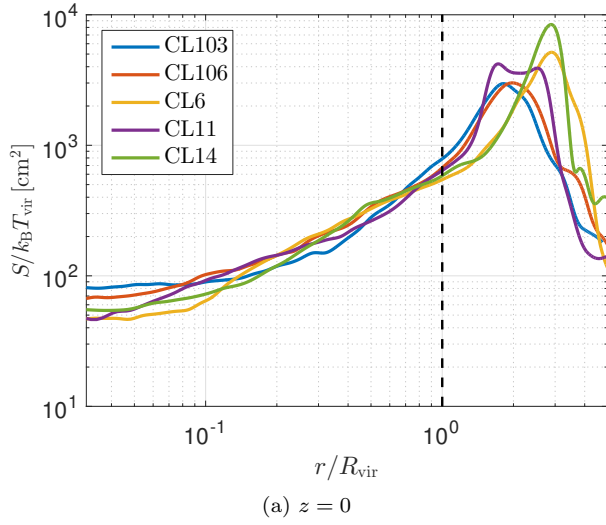


Figure 4. Entropy profiles averaged over spherical shells of the clusters shown above at $z = 0$ (a) and $z = 0.6$ (b). Dashed lines denote R_{vir} . The entropy is lowest in the cluster centre rising to a peak value near the shock before dropping sharply across the shock front. Since the shock front is not perfectly spherical the averaging leads to a widening of the entropy peak or in some cases to a double peak (CL11 in (a)).

what tricky, since the exact point in which the temperature drops is hard to determine. A similar predicament occurs for the pressure profile $P \propto \rho T$ since both the temperature and gas density rise towards the centre.

The entropy profiles on the other hand rise steadily from the low entropy core typical of galaxy clusters, reaching a peak value near the shock and drops off suddenly at the shock front. The drop in entropy is roughly one order of magnitude rather than a factor of 3–4, as can be seen in the maps, due to the smearing of the shock front when averaging over a spherical shell. The shape of the entropy profile with the distinctive maximum point and subsequent drop naturally lead to a ‘quick-and-dirty’ method of shock edge identification, based on the position of the local maxima of the entropy and the local minima of the entropy gradients, i.e. maximal negative gradient.

In Fig. 6 we show the entropy profile the cluster CL14

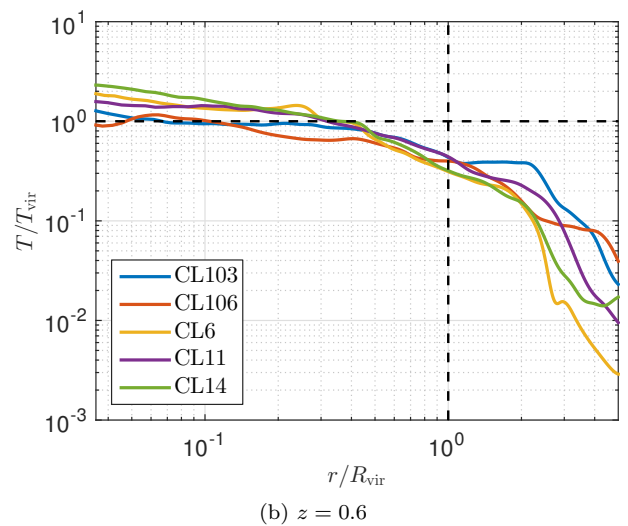
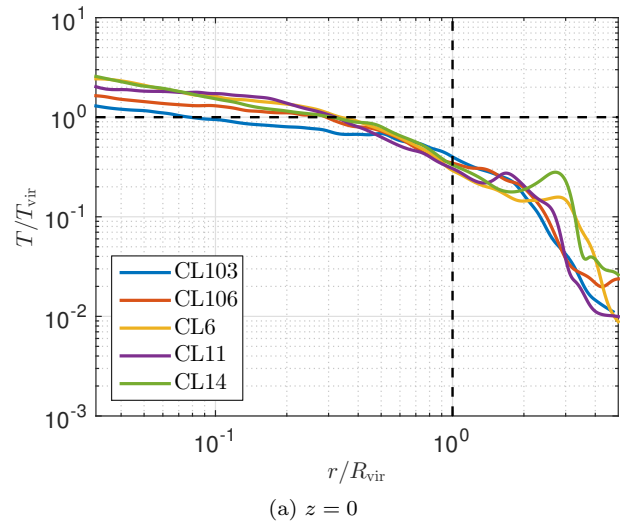


Figure 5. Temperature profiles averaged over spherical shells of the clusters shown above at $z = 0$ (a) and $z = 0.6$ (b). Dashed lines denote R_{vir} . The temperature rises sharply across the shock and then continues to climb gradually towards the centre where the temperature is highest. Due to the averaging, the drop in temperature is smeared, making it difficult to identify the position of the shock front.

at $z = 0$ and $z = 0.6$ and mark the radii of maxima in the entropy profile as well as the maximal negative gradients. We designate these radii as the shock edges, which are marked as black circles in Figs. 1c and 2c. As can be seen, in this particular case (as well as in many others), more than one local maxima was identified. This should come as no surprise since we have already noted that the shock front extends outwards to different distances in different directions.

As one can see, there is a certain redundancy in identifying both the local entropy maxima as well as the points of maximal negative gradient, since they are usually close by. However, when examining all the simulated systems we found that at times one method failed in identifying a shock where the other method succeeded, due to the intricate shape of the shock front. In addition, in this manner we can treat the maximal negative gradients as the shock front position and the local maxima as a lower bound to it. We find

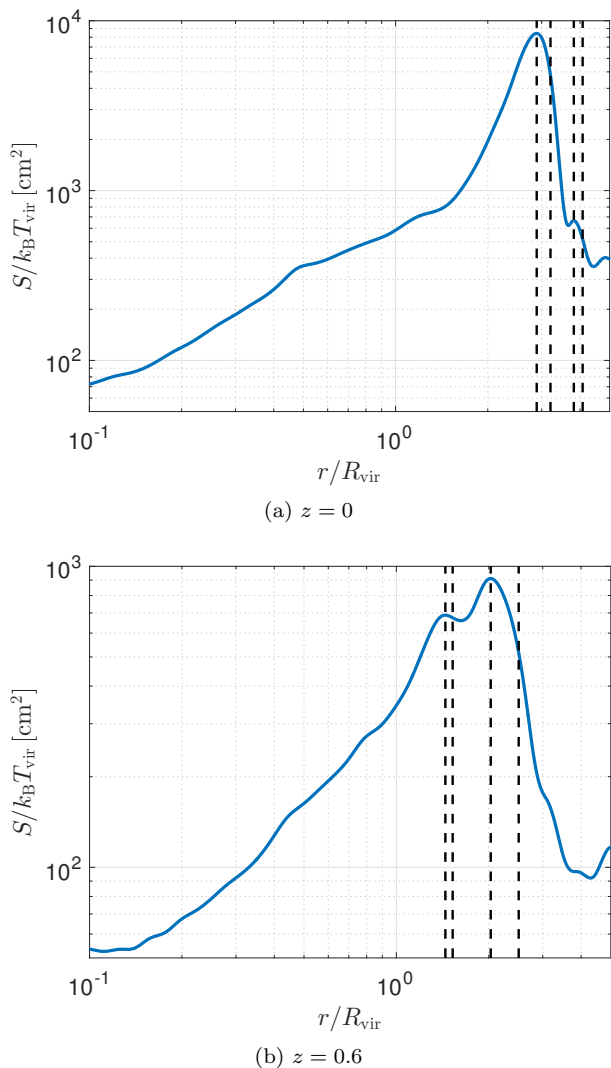


Figure 6. Entropy profile for cluster CL14 at $z = 0$ (a) and $z = 0.6$ (b). Dashed lines denote the points of local entropy maxima and local maxima of negative entropy gradient, which we use as a proxy for the shock edge.

that employing this simple method, of identifying both the entropy maxima and gradient maxima as a rough estimate of the position of the shock front to be perfectly adequate for our purposes. For each cluster, more than one ‘edge’ may be defined due to identification of both the entropy and entropy gradient maxima, as well as due to multiple instances of these features.

We performed this analysis on all systems, and verified the results by eye, removing specific cases which were obviously errors such as entropy maxima found close to the systems centre or identification of shocks in the large-scale structure very far from the virial shock. In Fig. 7 we show the shock edge positions, in units of R_{vir} , for all the clusters in our sample, both at $z = 0$ and $z = 0.6$ plotted versus the clusters’ virial mass. The green lines connect the edge estimation of a given system at $z = 0.6$ with the edge estimation of the same system at $z = 0$. We find that the shock front is always found beyond the virial radius and in all systems extends to well beyond twice the virial radius. One may make a case for a trend of decreasing $R_{\text{edge}}/R_{\text{vir}}$ with increasing

system size for the clusters at $z = 0$. However, attempts at generating an acceptable robust fit to these data points resulted in a very weak relation. In the $z = 0.6$ sample such a relation is non-existent.

Generally, the extent of the shock in units of R_{vir} is higher at $z = 0$ than at $z = 0.6$ but we find no special trend in the evolution of the shock edge for a given cluster, compared to the growth in the virial radius. Most clusters evolve such that the ratio is growing, and the growth in some cases is large, compared to a small decline in other cases.

Lau et al. (2015) find in a set of simulated clusters that the location of the accretion shock in units of R_{200} is dependent on the mass accretion rate of the clusters. The accretion shock radius is smaller in clusters with high mass accretion, a relation which holds in the redshift range $0 \lesssim z \lesssim 1.5$.

To examine this issue in our simulation suite we make use of a mass accretion parameter, defined in Diemer & Kravtsov (2014)

$$\Gamma \equiv \frac{\Delta \log M_{\text{vir}}}{\Delta \log(a)}, \quad (2)$$

where $a = (1 + z)^{-1}$ is the expansion parameter. We calculate Γ between the two epochs $a = 1$ ($z = 0$) and $a = 0.63$ ($z = 0.6$). In Fig. 8 we plot the shock edge estimation of the clusters at $z = 0$ (as shown in Fig. 7) as a function of Γ . In agreement with Lau et al. (2015) we also find that in clusters which experienced higher mass accretion between the two epochs the accretion shock is found closer to the virial radius.

4 RAM-PRESSURE STRIPPING OF THE GAS HALO

Now that it has been established that the virial shocks of clusters extend well beyond the virial radius, as early as $z = 0.6$, we can turn our attention to how this would affect the galaxies within the shock radius, specifically with a view towards the quenching of star formation.

The temperature of the area encompassed within the shock front is of order 10^6 – 10^8 K, (Figs. 1 and 2), and the velocity field is dominated by random motions, with the exception of the inflowing gas streams which is characterized by ordered inflow (Zinger et al. 2016).

One hydrodynamical mechanism which is known to affect galaxies in the ICM is ram-pressure stripping of the gas in the galaxy and its gas halo. The motion of the galaxy within the ICM generates a ram-pressure which, in some cases, can overcome the gravitational binding force of the satellite. The condition for gas stripping is

$$P_{\text{ram}} \geq \frac{F_{\text{grav}}}{dA}, \quad (3)$$

where dA is the cross-section area over which the ram-pressure affects the gas.

It has long been known that the motion of a satellite galaxy within the inner regions of the cluster can strip a galaxy of its gas (Gunn & Gott 1972), but we wish to assess the effect RPS has on an infalling galaxy, and its gas halo, within the accretion shock but *before* it reaches the virial radius of the cluster.

In this section we address the RPS of the gas halo which

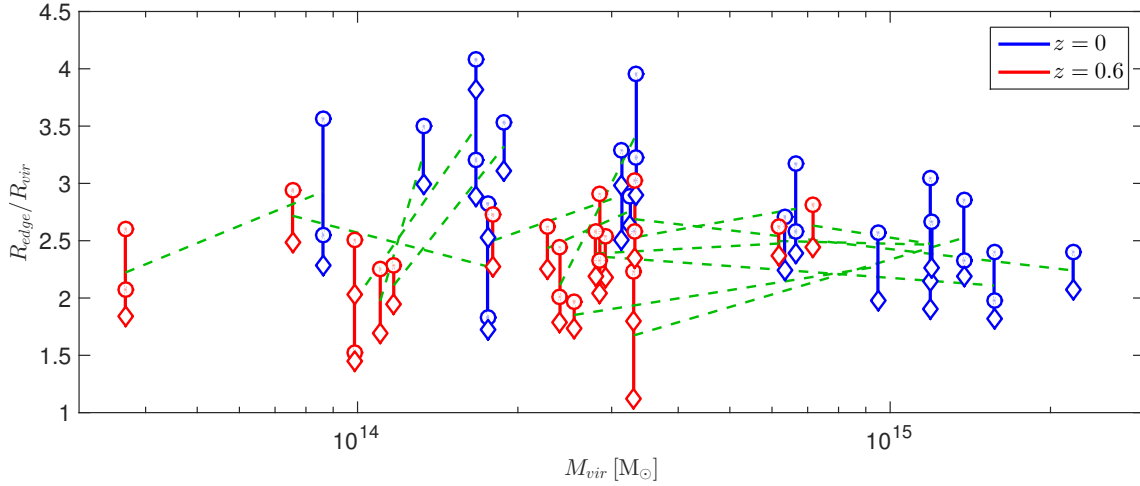


Figure 7. Shock edge estimation for all clusters at $z = 0$ (blue) and $z = 0.6$ (red) plotted versus the virial mass of the clusters. The edge estimations of a given cluster at the two redshifts are connected by the green lines. Edge estimations by entropy gradient are denoted by circles and entropy maximum by diamonds. All clusters exhibit shock edges which are well beyond the virial radius of the systems, extending to more than twice the virial radius in all cases.

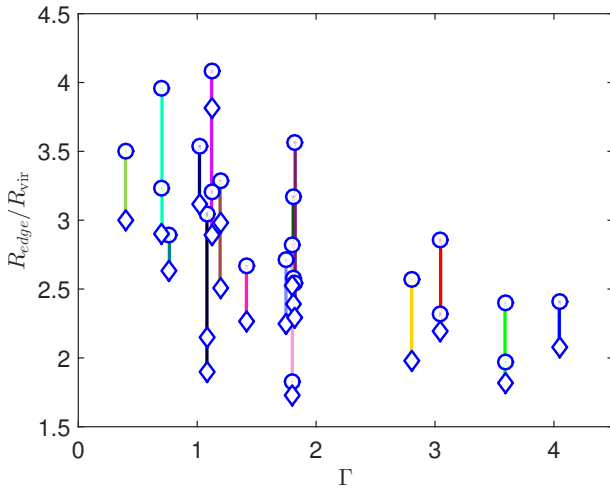


Figure 8. Accretion shock edge, in units of R_{vir} versus the mass accretion parameter Γ . As before, edge estimations by entropy gradient are denoted by circles and entropy maximum by diamonds. We find that in clusters with higher mass accretion rates the shock edge is closer to the virial radius.

surrounds the galaxy and is embedded in a dark matter subhalo. In §5 we examine the RPS expected for the gas found within the galactic disc.

The actual process of gas stripping by ram-pressure is a complicated one, as revealed by detailed hydrodynamical simulations (e.g. [Close et al. 2013](#)) which themselves are only approximations to the actual physical process. As a case in point, simulations do not usually include physical viscosity in the hydro-dynamic treatment and as such cannot properly capture the structure of the wake which forms around the moving object. The pressure in the wake reduces the effect of the ram-pressure induced by the motion of the object through the medium.

The gas in the hemisphere facing the ram-pressure is compressed and flows towards the edges, where it is swept

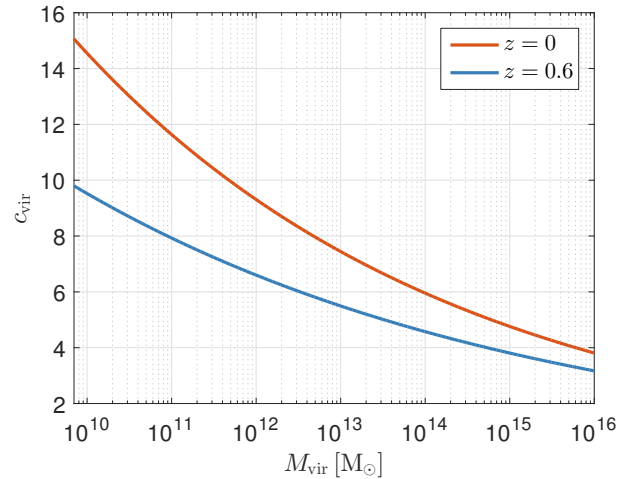


Figure 9. The relation between M_{vir} and c_{v} based on the analysis of [Muñoz-Cuartas et al. \(2011\)](#) for halos at $z = 0$ and $z = 0.6$, red and blue lines respectively.

back and stripped in turbulent tails. The gas distribution is deformed into a mushroom-like shape changing the area affected by the ram-pressure.

It is extremely challenging to construct an analytic model which will capture the intricacies of the RPS process. To overcome this hurdle, we employ a simple toy model to describe the satellite gas halo and its interactions with the ICM. In the model we will assume an upper limit for the binding gravitational force, so that the stripping is underestimated. If we still find substantial stripping in this limit we can be assured of the result despite the simplicity of the model.

4.1 Cluster and Satellite Models

The gaseous halo of a satellite or cluster, i.e. the ICM, resides within a dark matter halo which sets the gravitational

potential which in turns sets the thermodynamic properties of the gas. We make use of two simple density profiles to model the dark matter distribution for our clusters and satellites - the Isothermal Sphere profile and the NFW profile (Navarro et al. 1996, 1997). The former is used to obtain a simple analytic form for the stripping radius which highlights the dependence on the cluster and satellite masses. The latter, which is accepted as a reliable approximation for the dark matter distribution, is used to obtain a more precise numerical estimate for the stripping. To obtain the gaseous distribution we make the simple assumption that the gas is isothermal and in hydrostatic equilibrium within the dark matter potential.

4.1.1 The Isothermal Sphere

The density profile for the dark matter in an Isothermal Sphere model is given by

$$\rho_{\text{iso}}(r) = \frac{M_{\text{vir}}}{4\pi R_{\text{vir}}^3} \left(\frac{r}{R_{\text{vir}}} \right)^{-2}, \quad (4)$$

with the mass profile given by

$$M_{\text{iso}}(< r) = M_{\text{vir}} \left(\frac{r}{R_{\text{vir}}} \right). \quad (5)$$

Under the assumption of a hydrostatic isothermal gaseous component, the gas density profile, ρ_g , is set by the equation

$$\frac{k_B T_g}{\mu m_p} \frac{d \ln \rho_g}{dr} = - \frac{GM(r)}{r^2}, \quad (6)$$

where k_B is the Boltzmann constant, T_g is the gas temperature and $\mu m_p \simeq 0.59 m_p$ is the average particle mass (m_p being the proton mass). Under the assumption that the gas temperature is the same as the virial temperature of the halo, $T_g = T_{\text{vir}}$, solving eq. (6) results in $\rho_g \propto r^{-2}$, i.e. the gaseous distribution follows that of the dark matter and is also described by an Isothermal Sphere model. We therefore set the density and mass profiles for the gaseous distribution by $\rho_g = f_g \rho_{\text{iso}}$ and $M_g = f_g M_{\text{iso}}$ where f_g is the gas fraction defined by the ratio of the total gaseous mass within R_{vir} to the virial mass in the halo $f_g = M_{\text{gas}}/M_{\text{vir}}$.

The strength of the Isothermal Sphere model is its simplicity, which often allows for analytic solutions to toy-models leading to important insights as to the key-players of a given model. Of course, this is also its weakness - it is a poor approximation of the actual distribution of gas and dark matter seen in observations and simulations. In particular, the model over-predicts the density in the outskirts of clusters, beyond R_{vir} , which leads to an over-estimation of the RPS in these regions.

4.1.2 The NFW Model

The NFW model (Navarro et al. 1996, 1997) has long been accepted as a fair approximation for the dark matter distribution in halos. The density profile is given by

$$\rho_{\text{NFW}}(r) = \rho_u \delta_s \left(\frac{r}{r_s} \right)^{-1} \left(1 + \frac{r}{r_s} \right)^{-2}, \quad (7)$$

where ρ_u is the mean density of the universe, δ_s is an over-density parameter and r_s is the scale radius of the model.

The over-density parameter is given by

$$\delta_s = \frac{\Delta_{\text{vir}}}{3} \frac{c_v^3}{\mathcal{A}(1; c_v)}, \quad (8)$$

where $c_v \equiv R_{\text{vir}}/r_s$ and we define

$$\mathcal{A}(x; c_v) \equiv \ln(1 + c_v x) - \frac{c_v x}{1 + c_v x}. \quad (9)$$

Using eq. (1) one may recast the model using the parameters M_{vir} , R_{vir} and c_v

$$\rho_{\text{NFW}}(r) = \frac{M_{\text{vir}}}{4\pi R_{\text{vir}}^3} \mathcal{A}(1; c_v)^{-1} \left(\frac{r}{R_{\text{vir}}} \right)^{-1} \left(c_v^{-1} + \frac{r}{R_{\text{vir}}} \right)^{-2}. \quad (10)$$

The mass profile for the model is

$$M_{\text{NFW}}(r) = M_{\text{vir}} \frac{\mathcal{A}(r/R_{\text{vir}}; c_v)}{\mathcal{A}(1; c_v)}. \quad (11)$$

To use this model one must determine an additional parameter, namely c_v . Analysis of N -body simulations yields a power-law relation between M_{vir} and c_v as a function of redshift (Bullock et al. 2001a; Wechsler et al. 2002; Macciò et al. 2008). We use the relation found in Muñoz-Cuertas et al. (2011), reproduced in Fig. 9, to determine c_v for a given value of M_{vir} .

To set the gaseous distributions we solve the hydrostatic equation, eq. (6), under the same assumptions as before. The equation can be solved analytically (e.g. Makino et al. 1998; Brüggen & De Lucia 2008), resulting in a distribution which closely resembles a NFW profile for $0.1 R_{\text{vir}} < r < R_{\text{vir}}$, but possesses a density core for smaller radii. For radii of $r > R_{\text{vir}}$, the gas density drops off less rapidly than the dark matter density, and levels off at $r \gtrsim 2 R_{\text{vir}}$ a behavior which is *not* observed in real clusters (Finoguenov et al. 2001). In light of this, we opt instead to assume that the gas distribution follows that of the dark matter, i.e. $\rho_g = f_g \rho_{\text{NFW}}$ and $M_g = f_g M_{\text{NFW}}$ where once again f_g is the ratio of the gaseous mass to virial mass $f_g = M_{\text{gas}}/M_{\text{vir}}$. In this way the gas density in the outskirts of the cluster is not over-estimated, and the density profile of the satellite is similar to the results of the isothermal, hydrostatic gas distribution.

The NFW model is a better fit for observed distributions of dark matter and is expected to give better predictions for the RPS in the cluster outskirts. However, employing this profile in toy-models often results in implicit equations which entail a numerical solution. While more precise, it is sometimes harder to glean the important aspects from such a solution.

4.2 Tidal Stripping versus Ram-Pressure Stripping

Before continuing with assessing the stripping due to ram-pressure, we must ensure that it is indeed the dominant stripping mechanism in the region of interest, and that other stripping mechanisms, namely tidal stripping, do not void the basic assumptions of the model.

Tidal stripping occurs when the tidal forces acting on a satellite overcome the gravitational binding force of the satellite. Unlike RPS, which is a hydrodynamical process

that affects only the gas and leaves the dark matter halo intact, tidal stripping is a dynamical process which can remove the dark matter halo. If tidal stripping is effective in the region of interest, then modeling the gas halo as an Isothermal Sphere or by the NFW model may no longer be valid since the dark matter potential well which determines the gas properties of the halo may have been totally or partially removed (along with the gas).

To gauge the effectiveness of the tidal stripping we compare the tidal force acting on a gas element in the satellite halo and the gravitational force exerted by the satellite on said gas element. The tidal force is maximal along the line connecting the centres of the cluster and satellite. Perpendicular to that line, the tidal forces actually *compress* the satellite (Dekel et al. 2003). For a satellite whose centre is at a distance r from the cluster centre, the tidal force on a gas element of mass dm at a distance ℓ from the satellite centre (along the line connecting the centres) is

$$F_T = -\frac{GM_{\text{clust}}(r+\ell) dm}{(r+\ell)^2} + \frac{GM_{\text{clust}}(r) dm}{r^2} \quad (12)$$

and the gravitational force exerted by the satellite is

$$F_{\text{sat}}(r) = -\frac{GM_{\text{sat}}(|\ell|) dm}{|\ell|^3} \ell. \quad (13)$$

Combining eqs. (12) and (13) and assuming an Isothermal Sphere profile for both cluster and satellite results in the following equation for the tidal radius $\tilde{\ell}_t$ expressed in units of the satellite virial radius

$$\tilde{\ell}_t^2 - \mu^{1/3} \tilde{r} \tilde{\ell}_t - \tilde{r}^2 = 0, \quad (14)$$

where $\tilde{\ell}_t \equiv \ell_t/R_{\text{sat}}$, $\tilde{r} \equiv r/R_c$ and $\mu = M_{v,\text{sat}}/M_{v,\text{clust}}$. Solving the equations yields the tidal radius of the satellite as a function of the satellite position in the cluster

$$\tilde{\ell}_t = \tilde{r} \frac{\mu^{1/3}}{2} \left(1 + \sqrt{1 + 4\mu^{-2/3}} \right) \approx \tilde{r} \left(1 + \frac{\mu^{1/3}}{2} \right), \quad (15)$$

with the second, approximate relation valid when $\mu \ll 4^{3/2} = 8$, which is always the case since the mass of satellite haloes which host single galaxies in the cluster is of order 1 per cent of the cluster mass or lower.

We therefore find that the tidal radius of satellites found beyond the virial radius of the cluster is always larger than the virial radius of the satellite. We found this result to hold when both the satellite and cluster are modeled with an NFW profile as well. We can therefore safely conclude that tidal stripping is ineffective in the cluster outskirts.

4.3 Gauging the Mass Stripping

4.3.1 Ram-Pressure

A galaxy moving at a velocity of \vec{v}_{sat} within a gaseous medium of density ρ_{med} will be subjected to a ram-pressure of

$$P_{\text{ram}} = C_{\text{ram}} \rho_{\text{med}} (\vec{v}_{\text{sat}} - \vec{v}_{\text{med}})^2, \quad (16)$$

where \vec{v}_{med} is the local velocity of the medium and C_{ram} is a unit-less pre-factor.

For the motion of the satellite we will assume its speed is constant and equal to the virial velocity of the cluster

$$v_{\text{sat}} = \sqrt{\frac{GM_{v,\text{clust}}}{R_c}}. \quad (17)$$

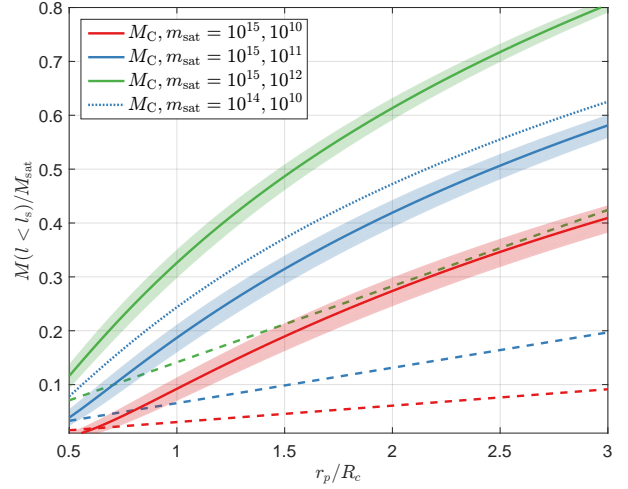


Figure 10. A simple toy-model for the amount of mass remaining in the gas halo of satellites undergoing RPS in the ICM of a $M_{v,\text{clust}} = 10^{15} M_{\odot}$ cluster, as a function of the position in the cluster in units of the cluster virial radius R_c . Solid lines represent the stripping for the NFW model, with the shaded regions corresponding to variations of up to ± 10 per cent in the values of both $c_{v,\text{clust}}$ and $c_{v,\text{sat}}$. Dashed lines show the stripping, for the same values of the satellite-to-cluster mass ratios, for the Isothermal Sphere model. The RPS efficiency parameter is set to $\epsilon' = 0.5$. Satellites lose more than 70 per cent of their gas halo mass before reaching the virial radius, with low-mass satellites losing as much as 90 per cent. For comparison, the blue dotted line shows the case of stripping in a $10^{14} M_{\odot}$ cluster with the same satellite-to-host mass ratio as the blue solid line (10^{-4}). The stripping in this case is reduced since both the cluster and satellite are more concentrated.

In addition we assume that the ICM is at rest compared to the satellite motion, ($v_{\text{med}} = 0$). While this is clearly not the case at every given point in the cluster, since the gas in the ICM is constantly in motion, it is true in an average sense if one takes into account that the velocity field of the ICM is dominated by random motions. Thus, as a satellite travels through the ICM, its velocity will at times be aligned with that of its surroundings and anti-aligned at other times (with the ram-pressure shrinking and growing accordingly), but on average the ICM velocity will be zero.

As can be seen in Fig. 14, this assumption appears to be valid with one important exception – motion along the gas streams falling into the cluster, where the velocity field is flowing coherently over large distances. We discuss the implications of this exception in §4.3.4.

Inserting eq. (17) into eq. (16) we use eqs. (4) and (10) to find the ram-pressure for the Isothermal Sphere,

$$P_{\text{ram}}(r) = \epsilon f_c \frac{G}{4\pi} \frac{M_{v,\text{clust}}^2}{R_c^4} \tilde{r}^{-2}, \quad (18)$$

and the NFW Model,

$$P_{\text{ram}}(r) = \epsilon f_c \frac{G}{4\pi} \frac{M_{v,\text{clust}}^2}{R_c^4} \left[\mathcal{A}(1; c_{v,\text{clust}}) \tilde{r} (c_{v,\text{clust}}^{-1} + \tilde{r})^2 \right]^{-1}, \quad (19)$$

where $\tilde{r} \equiv r/R_c$. In the above expressions, f_c is the cluster gas fraction, $M_{v,\text{clust}}$ and R_c are the virial mass and radius of the cluster respectively, and ϵ is a fudge-factor, added to

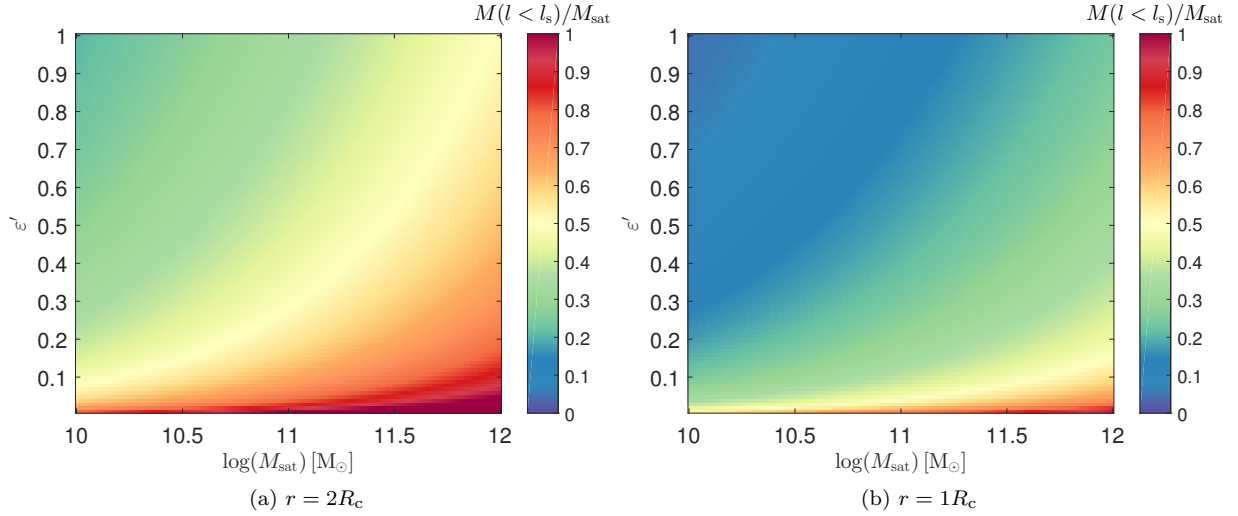


Figure 11. We explore the dependence of the simple NFW RPS toy-model on the efficiency parameter ε' , for a range of satellite masses within a $M_{\text{v,clust}} = 10^{15} M_{\odot}$ cluster. We examine the stripping for a satellite positioned at twice the cluster virial radius (a) and at the virial radius (b). At $2R_c$, low-mass satellites lose more than half the mass, even for low values of $\varepsilon' \gtrsim 0.1$. At $1R_c$, even high-mass satellites lose more than half their halo gas mass for low values of ε' , and low-mass galaxies are stripped to well below 20 per cent for most values of ε' .

incorporate any uncertainties in the assumptions we made in our model, e.g. motion with velocities different than the virial velocity, and which also accounts for C_{ram} .

4.3.2 Gravitational Binding

We wish to compare the ram-pressure to the binding gravitational force per unit area acting on the satellite gas halo and determine the amount of mass stripped from the satellite. While expressing the ram-pressure is relatively simple, as shown above, determining the correct form of the gravitational binding force for the appropriate mass elements affected is not so straightforward.

Ideally, one wishes to construct a simple spherical approximation for the binding force at a radius ℓ in the satellite which will lead to a definition of a stripping radius ℓ_s .

One option is to find the gravitational force which binds a spherical shell of width $d\ell$ at a given radius ℓ , divided by the cross section of that shell $dA = 2\pi\ell d\ell$

$$\frac{F_{\text{grav}}}{dA} = \frac{GM(\ell)}{\ell^2} \frac{\rho(\ell)4\pi\ell^2 d\ell}{2\pi\ell d\ell} = 2 \frac{GM(\ell)\rho(\ell)}{\ell}, \quad (20)$$

where $M(\ell)$ is the *total* mass profile and $\rho(\ell)$ is the gas density profile of the satellite. This approximation suggests that the ram-pressure ‘peels’ off spherical shells, like an onion, which is incongruous with the anisotropic nature of RPS. However, if the satellite halo is rotating with respect to its direction of motion, this approach may be justified.

Another option is to examine a cylindrical shell of radius ℓ and width $d\ell$ ($dA = 2\pi\ell d\ell$), oriented in the direction of motion of the satellite, and thus the direction of the ram-pressure force. McCarthy et al. (2008) employed this method by finding the maximal value of the restoring gravitational acceleration in the direction of the motion (and, by definition, the cylinder axis) as well as an upper limit of the projected surface density, resulting in an overestimation of

the binding force which ensures that one finds an upper limit to the stripping radius.

For a power-law spherically symmetric density profile $\rho \propto r^{-\alpha}$ the maximal restoring acceleration is¹

$$g_{\text{max}}(\ell) = \frac{GM(\ell)}{\ell^2} \sqrt{\frac{(\alpha-1)^{\alpha-1}}{\alpha^\alpha}}, \quad (21)$$

and the surface density is

$$\Sigma(\ell) = 2\rho(\ell)\ell \int_0^L (1+x^2)^{-\frac{\alpha}{2}} dx. \quad (22)$$

The upper limit of the integral is formally $L = \sqrt{R_{\text{vir}}/\ell - 1}$ but can be taken to $L \rightarrow \infty$ when the integral converges (or to some set scale otherwise) to achieve an upper limit for the surface density. The gravitational binding force is then

$$\frac{F_{\text{grav}}}{dA} = g_{\text{max}}(\ell)\Sigma_{\text{max}}(\ell) = \nu \frac{GM(\ell)\rho(\ell)}{\ell}, \quad (23)$$

where ν is a factor of order unity

$$\nu = 2\sqrt{\frac{(\alpha-1)^{\alpha-1}}{\alpha^\alpha}} \int_0^\infty (1+x^2)^{-\frac{\alpha}{2}} dx. \quad (24)$$

For an Isothermal Sphere profile we find $\nu = \pi/2$.

Yet another option is to assume that the gas halo is in hydro-static equilibrium within the gravitational potential of the dark matter halo of the satellite, and use the gas pressure as a proxy for the binding force per unit area. For a power-law density profile finding the pressure by integration of the hydro-static equation results in

$$P(\ell) = (2\alpha - 2)^{-1} \frac{GM(\ell)\rho(\ell)}{\ell}. \quad (25)$$

¹ Equation (21) is strictly correct for non-pathological cases of $\alpha \neq 3$. For $\alpha = 3$ it is still correct to equate the maximal acceleration with $GM(\ell)/\ell^2$ up to a numerical factor, which must be evaluated numerically.

For an Isothermal Sphere profile the pre-factor is $1/(2\alpha - 2) = 1/2$.

We find that employing several different methods of approximating the gravitational binding force all lead to an expression of the same form, namely

$$\frac{F_{\text{grav}}}{dA} = \kappa \frac{GM(\ell)\rho(\ell)}{\ell}, \quad (26)$$

with κ being a factor of order unity. While the above expression has been derived for a simple power-law density profile, it is reasonable to assume it is equally valid for more general density profiles, such as the NFW profile. Naturally, if one were to guess an approximation to the binding force per unit area based on a simple dimensional analysis, the above expression would be the result.

For the satellite models used in this work (§4.1) the gravitational binding force per unit area is

$$\frac{F_{\text{grav}}}{dA} = \kappa f_g \frac{G}{4\pi} \frac{M_{\text{v,sat}}^2}{R_{\text{sat}}^4} \tilde{\ell}^{-2} \quad (27)$$

and

$$\frac{F_{\text{grav}}}{dA} = \kappa f_g \frac{G}{4\pi} \frac{M_{\text{v,sat}}^2}{R_{\text{sat}}^4} \frac{\mathcal{A}(\tilde{\ell}; c_{\text{v,sat}})}{\mathcal{A}(1; c_{\text{v,sat}})^2} \left[\tilde{\ell} \left(c_{\text{v,sat}}^{-1} + \tilde{\ell} \right) \right]^{-2} \quad (28)$$

for the Isothermal Sphere and NFW models respectively where once again, $\tilde{\ell} \equiv \ell/R_{\text{sat}}$. In the equations above, we have assumed the gravitational potential is dominated by the dark matter component and neglected the gaseous component. Taking this component into account introduces an additional factor of $(1 + f_g)$. The effect of this additional factor on the stripping radius (eq. 29) for typical values of f_g is only of order several per cent.

4.3.3 Defining a Stripping Radius

To find the stripping radius we equate the ram-pressure, and the binding force. For the Isothermal Sphere model we use eqs. (18) and (27) to find the stripping radius, $\tilde{\ell}_s \equiv \ell_s/R_{\text{sat}}$, as a function of the satellite position within the cluster, $\tilde{r}_p \equiv r_p/R_c$

$$\tilde{\ell}_s = \sqrt{\frac{\kappa f_g}{\varepsilon f_c}} \left(\frac{M_{\text{v,sat}}}{M_{\text{v,clust}}} \right)^{\frac{1}{3}} \tilde{r}_p = \frac{1}{\sqrt{\varepsilon'}} \mu^{\frac{1}{3}} \tilde{r}_p, \quad (29)$$

making use of the relation $R_{\text{vir}} \propto M_{\text{vir}}^{\frac{1}{3}}$ (eq. 1). In this final form we combine the two fudge-factors κ and ε into a single parameter $\varepsilon' = \varepsilon/\kappa$ which incorporates all the uncertainties in the model. Low values of ε' reduce the effectiveness of the RPS mechanism. In addition, we hereafter make the reasonable assumption² that $f_c \simeq f_g$ and as before define the satellite to cluster mass ratio $\mu \equiv M_{\text{v,sat}}/M_{\text{v,clust}}$. Scaling by typical values allows us to estimate the value of the stripping radius

$$\tilde{\ell}_s \simeq 0.05 \left(\frac{\varepsilon'}{0.5} \right)^{-\frac{1}{2}} \left(\frac{M_{\text{v,sat}}}{10^{11}} \right)^{\frac{1}{3}} \left(\frac{M_{\text{v,clust}}}{10^{15}} \right)^{-\frac{1}{3}} \tilde{r}_p. \quad (30)$$

² The ratio f_g/f_c is of order unity, and enters the expression for the stripping radius as a power of 1/2. Any deviation from equality of the two gas fractions will have only a small effect on the stripping radius.

Under the assumption of an Isothermal Sphere profile for the satellite haloes, the value of $\tilde{\ell}_s$ also embodies the fraction of gas mass stripped from the halo (eq. 5). Equation (30) shows us that ram-pressure stripping of the halo gas is very efficient with $\gtrsim 95$ per cent of the gas having been stripped before the satellite reaches the virial radius.

The above result is hardly surprising due to the very simple gas model employed which is completely defined by a single parameter, in this case the virial mass of the halo, and for which the temperature and virial velocity are constants. This implies that the relation be governed completely by the mass ratio of the two bodies (and the free parameter ε') and that the model is completely scale free.

The Isothermal Sphere model is useful for achieving an explicit solution for the stripping, and shows that the halo gas in satellites is stripped almost completely when the satellite is at R_{vir} . However, as noted above, this is most likely an over-estimation of the stripping since the gas in this model is denser in the outskirts than more realistic profiles of the cluster density. A better approximation can be reached using the NFW model. Equating the ram-pressure with the gravitational binding force for an NFW model, eqs. (19) and (28), results in an implicit equation which can be solved numerically. Once a stripping radius is found, the mass remaining in the satellite can be calculated with eq. (11).

In Fig. 10 we show the amount of mass remaining in the gas halo of satellites of virial mass 10^{10} , 10^{11} and $10^{12} M_{\odot}$ within the ICM of a $10^{15} M_{\odot}$ cluster, both of which are modeled with the NFW profile. The solid line shows the result for an NFW profile where the concentration parameters of both host and satellite were set by the Muñoz-Cuartas et al. (2011) relation (Fig. 9), and the shaded region accounts for the results after varying the concentration parameter by as much as ± 10 per cent for both host and halo. In addition, the results of the Isothermal Sphere model for the corresponding mass ratios are also shown by the dashed lines.

We find that typical satellites in clusters will have already lost a substantial amount of their gas even at $2R_{\text{vir}}$, as much as 40 per cent for very massive satellites and 70 per cent (or more) for low mass satellites. A satellite at the virial radius of the cluster will retain only a small fraction of its initial gas halo, with values of 10 per cent and less for low-mass satellites. As expected, the Isothermal Sphere model can be seen to over-estimate the mass stripping, especially in the outer regions of the cluster.

An interesting feature can be seen when comparing the results for the $10^{11} M_{\odot}$ satellite in a $10^{15} M_{\odot}$ host (solid blue line) to the results for a $10^{10} M_{\odot}$ satellite in a $10^{14} M_{\odot}$ cluster (dotted blue line). Though the satellite-host mass ratio is identical for both cases, the stripping is markedly weaker for the lower mass host. This is due to the fact that the concentration parameter is higher for lower mass halos (Fig. 9). The relative drop in density (at a given position in units of R_{vir}) is larger for a more concentrated host halo, reducing the ram-pressure. In addition, a more concentrated satellite is more tightly bound and therefore harder to strip.

In Fig. 11 we explore the dependence of the NFW model on the stripping effectiveness parameter ε' . For a cluster of $M_{\text{v,clust}} = 10^{15} M_{\odot}$ we plot the mass remaining within the gas halo at the virial radius of the cluster and at twice the distance, for a range of satellite masses and ε' values. We can see that even for very weak stripping, i.e. low values of

$\varepsilon' \simeq 0.1$, all but the most massive satellites lose more than 60 per cent of their mass at the virial radius.

Since we find that the stripping is effective even for low values of ε' we can rest assured that the various approximations made in our simple model, especially with respect to the gravitational binding force (§4.3.2), do not change the conclusion that the gas haloes lose all but a small fraction of their initial mass *before* they reach the virial radius of the cluster for the first time.

4.3.4 Ram-Pressure Stripping in Simulated Clusters

We now make use of our simulated cluster systems to gauge the stripping of the satellite gas halo in a more realistic setting. The satellite is still modeled with a NFW profile, moving at the virial velocity, but the gas density of the ICM is taken directly from the simulations.

In Fig. 12 we show representative examples for a $10^{11} M_{\odot}$ satellite halo in 3 simulated clusters (CL101, CL3, CL14) at $z = 0$ and $z = 0.6$. The ram-pressure exerted by the cluster gas, eq. (16), is calculated using the spherically averaged density profile from the simulation. The lowest value of the shock edge, as defined in §3.2, is also shown. For comparison, the stripping due to a cluster with an NFW profile of the same virial mass is also shown. The concentration parameter c_v is defined here by the c_v - M_{vir} relation and *not* calculated from the dark matter distribution in the simulation.

The stripping in the simulated clusters is very similar to the results of the simple NFW toy-model. This indicates that the NFW model is indeed a very good approximation for the gas density profile of the cluster, at least for these simulated clusters. The stripping is more effective for higher mass clusters, for which the satellite retains less than 20 per cent of its gas mass at R_c , but even for the low-mass cluster, the satellite loses more than 60 per cent of its gas mass. The stripping at the location of the shock edge is already strong enough to strip over 60 per cent of the halo gas, at least for the high-mass clusters.

In Fig. 13 we show the stripped mass of a $M_{\text{v,sat}} = 10^{11} M_{\odot}$ satellite calculated at a position within the cluster of $2R_c$ and $1R_c$ for all the clusters in the simulation suite at $z = 0$ and $z = 0.6$. The mass dependence of the effectiveness of the stripping is evident here. Even at $2R_c$ the satellite halo in the high mass halo loses over half of the gas and at $1R_c$, only 20 per cent of the gas still remains. For the low-mass halos, more than half the halo gas has been removed at R_c . At first glance it would seem surprising that the stripping seems less effective at $z = 0$ than at $z = 0.6$ but one must keep in mind that the comparisons in Figs. 12 and 13 are performed at the virial radius, which changes by a factor of 2 between the two epochs. The density at the virial radius at $z = 0.6$ is higher by a factor of 2 than at $z = 0$, thus the stripping is greater, but in terms of absolute distance, at $z = 0$ the stripping occurs at twice the distance. In addition, the concentration of both clusters and satellites is lower at $z = 0.6$ (Fig. 9) which also leads to more effective stripping.

In Fig. 14 we see the effect of the gas stripping within a representative cluster (CL103), as well as a representation of the velocity field in the cluster. The left and right panels show the cluster at $z = 0$ and $z = 0.6$ respectively. In

Figs. 14a and 14b we show the amount of mass stripped from a $M_{\text{v,sat}} = 10^{11} M_{\odot}$ halo at every point within the halo. As can be seen, the halo is stripped to between 70 to 90 per cent of its original mass at the virial radius. In fact, simply entering the shocked ICM leads to stripping of 30 to 50 per cent of the mass.

It is important to note that in one respect the results shown in Fig. 14 may be misleading – stripping along the gas streams flowing into the clusters. This is especially pertinent since most galaxies are expected to accrete onto the cluster via these streams. The density in the streams is high compared to the surrounding ICM, so the stripping appears enhanced in the streams. However, the ram-pressure is a result of the motion of the satellite relative to the surrounding medium, eq. (16). Within the ICM, which is characterized by random motions, one does not expect the satellite motion to be correlated to its surrounding. Clearly this is not the case within the streams, which exhibit highly ordered flows. This is especially apparent in Fig. 14b.

If a satellite travels along a stream and its velocity is similar to the surrounding stream velocity, the RPS would be attenuated and the satellite could reach the virial radius or even the cluster centre, while suffering only minor mass loss. Thus, along the streams the RPS may be stronger or weaker depending on whether or not the drop in ram-pressure due to the satellite co-moving with the streams is compensated by the increased density in the stream.

The results of our model are in agreement with those of Bahé et al. (2013) who employ a cosmological SPH simulations in which individual satellites can be followed and their gas content monitored. Their results show that the hot gas haloes are removed by the time the satellites reach the cluster virial radius. In these simulations, the effect of stripping seems to be enhanced in the filaments, with the increased density within the stream outweighing the lower contribution of the relative velocity.

5 RAM-PRESSURE STRIPPING OF THE GALACTIC DISC

In the previous section we demonstrated that ram-pressure can be a very efficient mechanism for stripping the gas haloes of satellites well outside the virial radius, thus removing the gas reservoir which can cool on to the galaxy. We now address the possibility of removing the gas held within a galactic disc by ram-pressure stripping.

To do so, we wish to compare the force exerted by the ram-pressure on a gas element *within* the galaxy disc with the gravitational binding force exerted by the galaxy, as was formulated in eq. (3). Once again we construct a simple toy-model to evaluate the effectiveness of RPS on the gas in the disc.

In our simple toy-model we make the following assumptions:

- a) The galaxy is modeled as a thin exponential disc³ of stars and gas and a spherical stellar bulge.

³ In order to gauge the stability of the disc we extend the stellar disc model to account for the vertical structure of the disc. How-

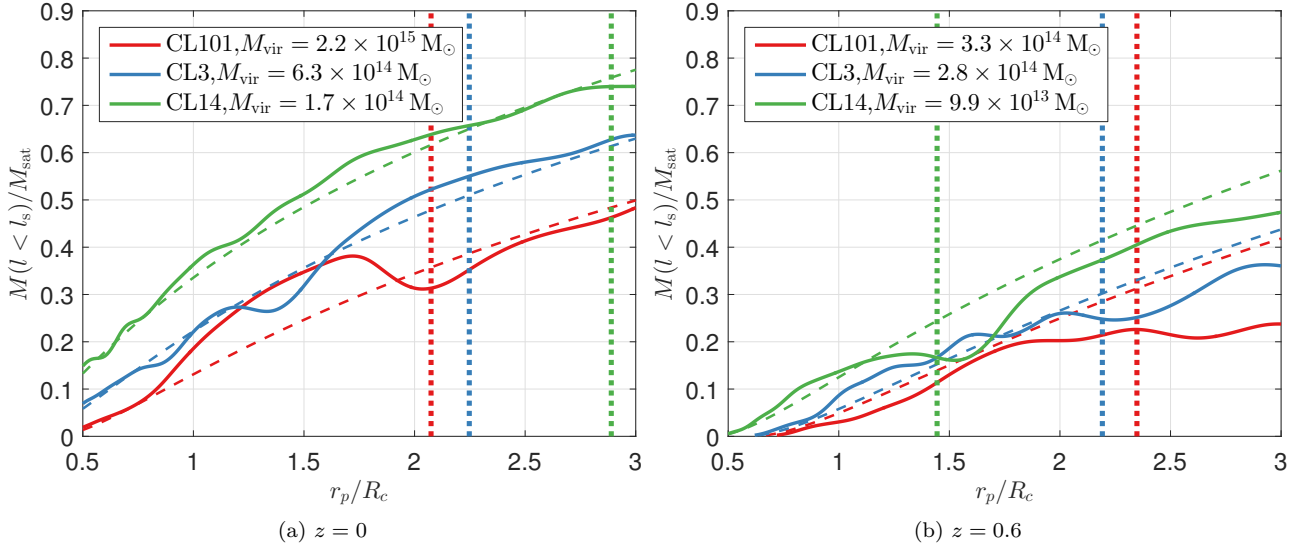


Figure 12. The remaining gas mass of a $M_{\text{vir}} = 10^{11} M_{\odot}$ satellite halo (modelled with an NFW profile) in 3 representative simulated clusters: CL101 (blue), CL3 (red) & CL14 (green). The ram-pressure of the cluster is calculated by using the spherically averaged gas density profile, and assuming the satellite travels at the virial velocity of the cluster. In this calculation we have assumed $\varepsilon' = 0.5$. The dashed lines show in comparison the remaining mass assuming a NFW model for the cluster gas (as in Fig. 10). We present the results for the 3 clusters at $z = 0$ (a) and $z = 0.6$ (b). The dotted lines denote the lowest value of the shock edge as defined in §3.2 (Fig. 7). The stripping in the simulated clusters is very similar to the NFW toy-model. The stripping is very effective in the high-mass clusters, removing more than 80 per cent of the gas before the satellites reach the virial radius. The stripping in the lower mass clusters is less effective but still more than 60 per cent of the gas is removed by the time the satellite reaches the virial radius of the cluster.

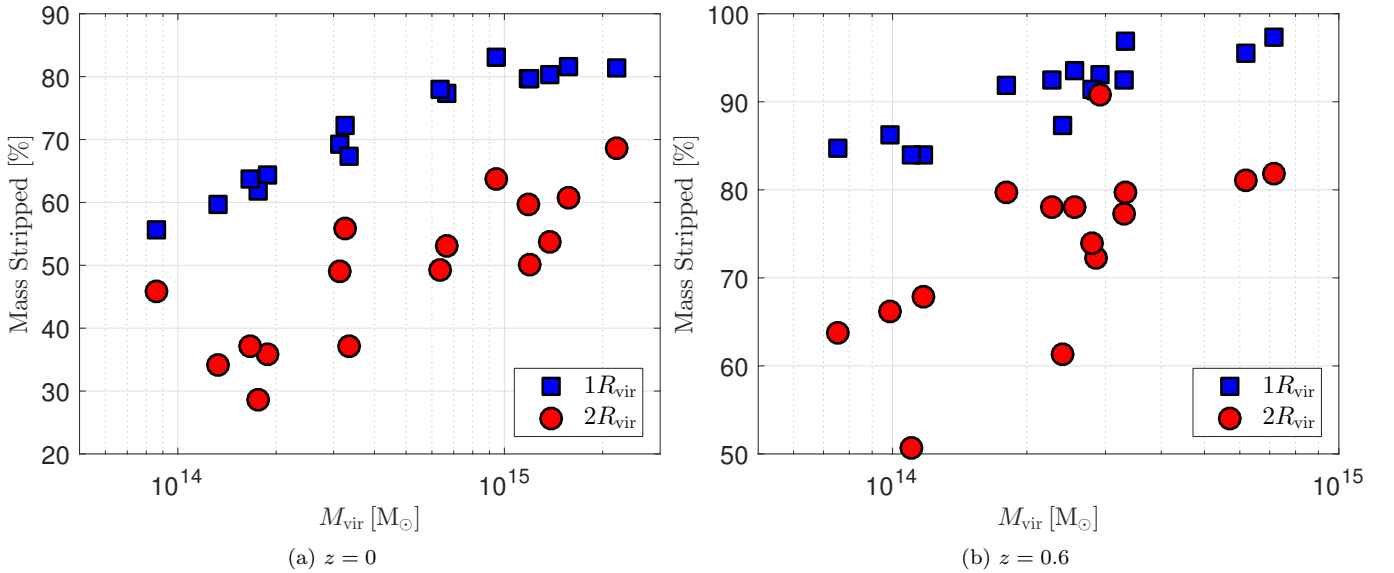


Figure 13. The total amount of gas stripped from a NFW satellite halo of $M_{\text{v,sat}} = 10^{11} M_{\odot}$ at twice the virial radius of the cluster ($2R_c$, red circles) and at the virial radius of the cluster ($1R_c$, blue squares) in all the clusters of the simulation suite at $z = 0$ (a) and $z = 0.6$ (b). The effectiveness of the stripping in our simple model is dependent on the cluster mass, with the satellite losing about 60 per cent of its gas mass in the low-mass clusters and as much as 80 per cent for the high mass clusters. The stripping is more effective at $z = 0.6$, due to the higher densities found at the virial radius and the lower concentrations of satellites at that epoch.

b) The centre of mass velocity of the galaxy relative to the ICM is perpendicular to the galactic disc plane, thus the ef-

ever, we do not consider the vertical structure when calculating the RPS.

fect of the ram-pressure is maximal. Several numerical studies (Quilis et al. 2000; Roediger & Brüggen 2006; Jáchym et al. 2009) found that except when the disc is nearly edge-on compared to its direction of motion, RPS is largely insensitive to the inclination angle with respect to the direction of motion.

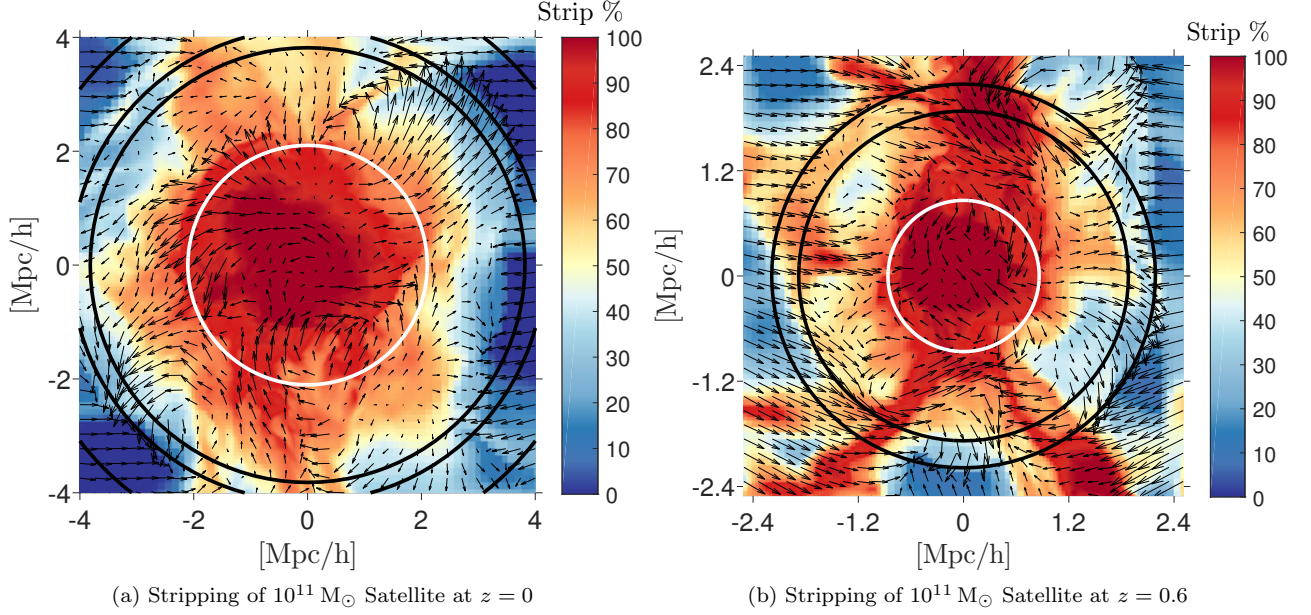


Figure 14. Stripping of the gaseous halo of a satellite calculated based on the simulated gas density in the ICM of the cluster CL103 at $z = 0$ (left) and $z = 0.6$ (right). The RPS effectiveness parameter is assumed to be $\varepsilon' = 0.5$. The figures show the percentage of gas mass stripped from a $M_{\text{vir}} = 10^{11} M_{\odot}$ satellite at each point in the cluster. We see that already in the vicinity of the shock front (marked by black circles) the satellite will be stripped of at least 30 per cent of its mass. At the virial radius of the cluster (white circle) the satellite has lost between 70 to 90 per cent of its halo gas mass. The black arrows show the velocity field which highlights the inflow along the high density streams.

We now describe the galaxy model employed to calculate the gravitational binding force per unit area within the disc plane.

5.1 Disc Galaxy Model

Our galaxy model is comprised of three galactic components: a stellar disc and a gaseous disc, both modeled as thin exponential discs, and a stellar bulge component, all of which are embedded within a dark matter halo. In the following sections we present the main characteristics of the model.

5.1.1 Stellar Disc

We model the stellar disc as an exponential disc, with surface density and mass of

$$\Sigma_{\text{stars}}(R) = \Sigma_s e^{-\frac{R}{R_s}} \quad (31)$$

$$M_{\text{stars}}(R) = M_s \left[1 - e^{-\frac{R}{R_s}} \left(1 + \frac{R}{R_s} \right) \right], \quad (32)$$

where R denotes the distance from the disc centre in the plane of the disc, M_s is the stellar mass in the disc and R_s is the exponential scale radius. The surface density parameter Σ_s is related to the other parameters via the relation $\Sigma_s = M_s / (2\pi R_s^2)$.

The gravitational acceleration in the plane of a thin,

exponential disc is (Binney & Tremaine 2008, Ch. 2.6)

$$\begin{aligned} g(\tilde{R}) &= -\frac{d\Phi}{d\tilde{R}} \\ &= -\pi G \Sigma_s \tilde{R} \times \\ &\quad \left[I_0 \left(\frac{\tilde{R}}{2} \right) K_0 \left(\frac{\tilde{R}}{2} \right) - I_1 \left(\frac{\tilde{R}}{2} \right) K_1 \left(\frac{\tilde{R}}{2} \right) \right], \end{aligned} \quad (33)$$

where I_ν and K_ν are the modified Bessel functions of the first and second kind and we have defined $\tilde{R} = R/R_s$. In the interest of convenience we introduce the following function

$$B_\nu(x) = I_0 \left(\nu \frac{x}{2} \right) K_0 \left(\nu \frac{x}{2} \right) - I_1 \left(\nu \frac{x}{2} \right) K_1 \left(\nu \frac{x}{2} \right), \quad (34)$$

such that eq. (33) is now

$$g(\tilde{R}) = -\pi G \Sigma_s \tilde{R} B_1(\tilde{R}). \quad (35)$$

5.1.2 Gaseous Disc

The gaseous disc is also modeled as an exponential disc (Bigiel & Blitz 2012) with a mass of M_g and a scale radius R_g . We present these parameters in units of the stellar disc parameters as $f_{\text{gs}} = M_g/M_s$ and $\beta = R_s/R_g$. By this definition, values of $\beta > 1$ correspond to a gaseous component which is more *compact* than the stellar component and values of $\beta < 1$ result in a gaseous disc which is more *extended* than the stars.

The surface density of the gas disc is therefore (see eq. 31)

$$\Sigma_{\text{gas}}(\tilde{R}) = \Sigma_g e^{-\frac{\tilde{R}}{\beta}} = \Sigma_s f_{\text{gs}} \beta^2 e^{-\beta \tilde{R}}, \quad (36)$$

from which the mass profile is found to be

$$M_g(< \tilde{R}) = M_s f_{\text{gs}} \left(1 - e^{-\beta \tilde{R}} \left(1 + \beta \tilde{R} \right) \right). \quad (37)$$

The gas disc contribution to the gravitational acceleration is

$$g_{\text{gas}}(\tilde{R}) = -\pi G \Sigma_s f_{\text{gs}} \beta^3 \tilde{R} B_\beta(\tilde{R}). \quad (38)$$

5.1.3 Stellar Bulge

To model the stellar bulge component we use the Hernquist profile (Hernquist 1990) for which the density profile is

$$\rho(r) = \frac{M_b}{2\pi} \frac{R_b}{r} \frac{1}{(R_b + r)^3}, \quad (39)$$

where the stellar mass of the bulge is M_b and the scale radius is R_b . As before, we recast the bulge model parameters in terms of the stellar disc parameters, $f_{\text{bs}} = M_b/M_s$ and $\xi = R_s/R_b$, noting f_{bs} is essentially the ‘Bulge-to-Disc’ stellar mass ratio. In many cases, observed galaxies are classified according to the ‘Bulge-to-Total’ stellar mass ratio. The relationship between the two is

$$\frac{B}{T} \equiv \frac{M_b}{M_s + M_b} = \frac{f_{\text{bs}}}{f_{\text{bs}} + 1}. \quad (40)$$

The gravitational acceleration exerted by the bulge (in the disc plane) is thus

$$g_{\text{bulge}}(\tilde{R}) = -\frac{GM_b}{(R_b + r)^2} = -\frac{2\pi G \Sigma_s f_{\text{bs}} \xi^2}{(1 + \xi \tilde{R})^2}. \quad (41)$$

5.1.4 Dark Matter Halo

For a spherically symmetric dark matter halo, for which the mass profile is $M_H(r)$ the contribution to the gravitational acceleration will be

$$g_H(r) = \frac{GM_H(r)}{r^2} \rightarrow g_H(\tilde{R}) = 2\pi G \Sigma_s \frac{M_H(\tilde{R})}{M_s} \tilde{R}^{-2}. \quad (42)$$

We assume an NFW model for the dark matter halo as described in detail in §4.1.2.

5.1.5 Full Model

For the fully assembled galaxy, the total gravitational acceleration is the sum of the contributions of all three components

$$g_{\text{gal}}(\tilde{R}) = -\pi G \Sigma_s \tilde{R} \times \left[B_1(\tilde{R}) + f_{\text{gs}} \beta^3 B_\beta(\tilde{R}) + \frac{2f_{\text{bs}} \xi^2}{(1 + \xi \tilde{R})^2} \right]. \quad (43)$$

The full acceleration is obtained by adding the contribution of the halo (eq. 42) to the above expression. As one would expect, at very large distances the acceleration drops as $g_{\text{gal}} \propto r^{-2}$.

In Fig. 15 we show a decomposition of the contributions of the various components of the galaxy and halo to the gravitational acceleration of a representative $M_s = 10^{10} M_\odot$ galaxy. The gaseous component is defined by a gas fraction of $f_{\text{gs}} \simeq 0.3$ and with $\beta \simeq 0.9$. The bulge-to-disc mass ratio is $f_{\text{bs}} \simeq 0.2$ with $\xi = 3.6$, and thus can be seen to dominate the acceleration in the centre of the galaxy. In addition, the galaxy is embedded in a dark matter NFW model halo with

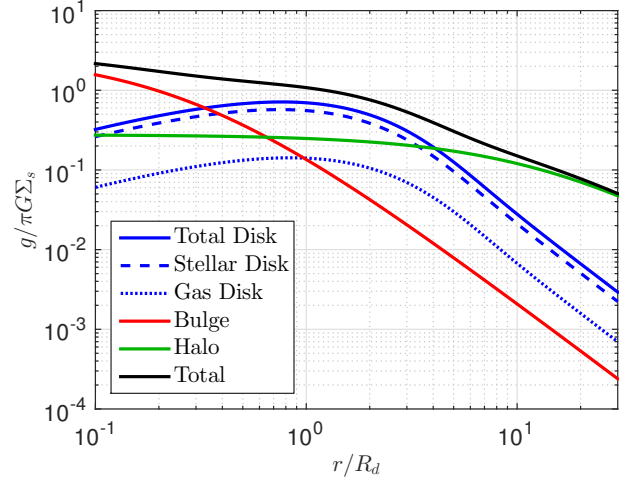


Figure 15. Decomposition of the gravitational acceleration into the contributions from the various components in a $M_s = 10^{10} M_\odot$ galaxy. The total disc contribution (solid blue) is divided into the stellar disc contribution (dashed blue) and the gaseous disc ($f_{\text{gs}} \simeq 0.2$, $\beta \simeq 0.9$) contribution (dotted blue). The bulge component ($f_{\text{bs}} \simeq 0.11$, $\xi = 3.6$) can be seen to dominate the acceleration in the centre of the galaxy (red). The galaxy is embedded in a $M_{\text{vir}} = 5.7 \times 10^{11} M_\odot$, $c_{\text{vir}} \simeq 9.5$ NFW dark matter halo (green). The total profile (black) is also shown. The halo becomes the dominant component at $r \gtrsim 5R_s$, where it becomes an important contribution to the disc stability.

$M_{\text{vir}} = 4.8 \times 10^{11} M_\odot$ and $c_{\text{vir}} \simeq 10$. The halo contribution is comparable to that of the disc in the inner parts of the galaxy $r \lesssim R_s$ but becomes the dominant component at $r \gtrsim 5R_s$. This has important consequences on the stability of the disc.

The force per unit area affecting the gas is $F = (g_{\text{gal}} + g_H) \Sigma_{\text{gas}}$. The total force per kpc^2 is therefore

$$F(\tilde{R}) = -\pi G \Sigma_s^2 f_{\text{gs}} \beta^2 e^{-\beta \tilde{R}} \tilde{R} \times \left[B_1(\tilde{R}) + f_{\text{gs}} \beta^3 B_\beta(\tilde{R}) + \frac{2f_{\text{bs}} \xi^2}{\tilde{R} (1 + \xi \tilde{R})^2} + \frac{2M_H(\tilde{R})}{M_s \tilde{R}^3} \right], \quad (44)$$

which we separate into a unit-less function $\mathcal{F}(\tilde{R})$ describing the spatial dependence of the force and a constant factor comprised of the relevant galaxy parameters

$$\mathcal{F}(\tilde{R}) = \frac{F(\tilde{R})}{\pi G \Sigma_s^2 f_{\text{gs}}}. \quad (45)$$

As noted earlier, the true complexities of the RPS process are beyond the scope of a simple analytic model. In reality, the gas will be pushed out and the disc will be warped by the ram-pressure (e.g. Vollmer et al. 2008b,a).

We make a simplifying assumption that the total gravitational binding force is represented by the force acting on a gas element in the plane of the disc. In order to estimate the error implicit in this assumption we consider a thick disc model to find the acceleration in the z direction. In a more realistic thick disc, the gravitational binding force on a gas element dm at a position (R, z) , where R is the distance from the centre in the plane of the disc and z is the perpendicular

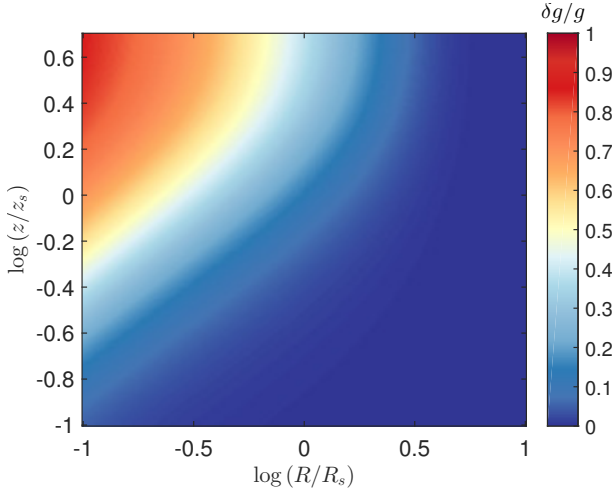


Figure 16. The fractional error incurred by neglecting the z component of the gravitational acceleration as a function of $\tilde{R} = R/R_s$ and z/z_s . We find that beyond R_s we may approximate the gravitational binding force using the component within the disc plane, neglecting the z component which accounts for less than 10 per cent.

distance from the disc plane will be

$$F_g = \sqrt{g_R^2 + g_z^2} dm, \quad (46)$$

where g_R and g_z are the gravitational acceleration components parallel and perpendicular the disc.

In order to estimate the error of neglecting the acceleration in the z direction, we employ the Isothermal Sheet model which assumes that the vertical distribution of the stellar disc is locally isothermal such that the distribution function of stars in the z direction at every R is Maxwellian (Spitzer 1942; Mo et al. 2010). The resulting gravitational acceleration perpendicular to the disc in this model is given by

$$g_z(R, z) = \frac{M_s}{R_s^2} e^{-\frac{R}{R_s}} \tanh\left(\frac{z}{2z_s}\right), \quad (47)$$

where z_s is the scale height of the disc.

In Fig. 16 we examine the fractional error in the gravitational acceleration incurred by neglecting the z -component defined as

$$\frac{\delta g}{g} = 1 - \frac{g_R}{\sqrt{g_R^2 + g_z^2}}. \quad (48)$$

As can be seen, in the regime relevant for stripping $R \gtrsim R_s$, $z < z_s$, ignoring the vertical component of the acceleration leads to negligible errors in estimating the gravitational binding, and the total acceleration can be approximated by the acceleration in the disc plane.

5.2 Constructing Mock Galaxy Catalogs

The disc model presented above is fully described by 2 primary parameters M_s, R_s of units M_\odot and kpc respectively, while the rest of the parameters, namely f_{gs}, β, f_{bs} and ξ , are unit-less ratios with respect to these parameters.

All together, this results in a rather large parameter space which we need to explore to find the effectiveness of

RPS in removing gas from the galactic disc. To contend with this challenge, we generate a large catalog of $\gtrsim 10^4$ mock galaxies, in which the different parameters have been chosen randomly, thus allowing us to investigate the effects of RPS on galaxies of many different attributes.

In the interest of achieving a physically motivated choice for these parameters, we employ the model presented in Mo et al. (1998) to relate the scale radius R_s to the stellar mass of the disc and the properties of the host halo. The model assumes that the gas which formed the stellar disc conserves its specific angular momentum during the formation process, and more importantly, that the specific angular momentum was equal to that of the dark matter of the host halo in which the galaxy formed. Dekel et al. (2013) and Danovich et al. (2015) find that the spin of a galaxy and its host dark matter halo are indeed very similar (up to a factor of 2), despite the very different history of angular momentum buildup by gas and dark matter. Observations of the relation between R_s of the galaxy and R_{vir} of the halo are in general agreement with this model (Kravtsov 2013). While the original model assumed that all the gas ended up as stars in a stellar disc and bulge, we have extended it to allow some of the gas to form a gaseous disc component.

We relate the properties of the galaxy with the dark matter halo by expressing the angular momentum of the disc J_d as a fraction j_d of the total angular momentum of the dark matter halo J , such that $J_d = j_d J$. The angular momentum of a dark matter halo can be expressed by the unit-less spin parameter as defined by Bullock et al. 2001b

$$\lambda' = \frac{J}{\sqrt{2} M_{\text{vir}} V_{\text{vir}} R_{\text{vir}}}. \quad (49)$$

The angular momentum of the disc can be calculated by⁴

$$\begin{aligned} J_d &= \int_0^{R_{\text{vir}}} \Sigma_T(R) R V_c(R) 2\pi R dR \\ &= 2\pi \Sigma_s R_s^3 \int_0^{\frac{R_{\text{vir}}}{R_s}} x^2 \left(e^{-x} + f_{gs} \beta^2 e^{-\beta x} \right) V_c(x R_s) dx \\ &= M_s R_s V_{\text{vir}} \tau^{-1}, \end{aligned} \quad (50)$$

where we have used the total disc surface density $\Sigma_T = \Sigma_{\text{stars}} + \Sigma_{\text{gas}}$ (eqs. 31 and 36), and the circular velocity of the disc is given by V_c . We define

$$\tau^{-1} = \int_0^\infty x^2 \left(e^{-x} + f_{gs} \beta^2 e^{-\beta x} \right) \frac{V_c(x R_s)}{V_{\text{vir}}} dx, \quad (51)$$

setting the upper limit for the integral to ∞ since the integrand drops exponentially, and the ratio R_{vir}/R_s is usually of order ~ 10 –100.

The circular velocity needed to calculate eq. (51) is determined by the *entire* system, i.e. stars, gas bulge and dark matter. In calculating it one must take into account that the sinking of baryons to the centre of the halo to form the galaxy leads to a contraction of the dark matter in the centre of the halo. We assume that the halo response to the assembly of the disc is adiabatic (Blumenthal et al. 1986; Flores et al. 1993; Dalcanton et al. 1997), and therefore the angular momentum of individual dark matter particles is conserved.

⁴ We assume the stellar bulge has negligible angular momentum.

Combining eqs. (49) and (50) the scale radius of the disc can be expressed as

$$R_s = \sqrt{2\lambda'} \left(\frac{j_d}{m_d} \right) (1 + f_{gs}) \tau R_{\text{vir}}, \quad (52)$$

where m_d is the fraction of total mass initially in the halo found in the galactic disc

$$m_d = \frac{M_s + M_g}{M_{\text{vir}}} = \frac{M_s}{M_{\text{vir}}} (1 + f_{gs}), \quad (53)$$

and $\tau = \tau(M_s, R_s, f_{gs}, \beta, f_{bs}, \xi, m_d, c_v)$ is a function of the model parameters. The implicit equation eq. (52) can be solved iteratively once the values of the disc, bulge and halo parameters have been determined.

To implement this procedure, we must select the properties of the host dark matter halo for each galaxy (M_{vir}, c_v and λ'), the values of the parameters relating the halo to the galaxy (j_d and m_d) and of course the galaxy properties ($M_s, f_{gs}, \beta, f_{bs}$ and ξ). The values of these parameters are randomly chosen for each galaxy based on physical or observational considerations as well as wisdom gleaned from simulations.

5.2.1 Setting the Galaxy Parameters

To achieve a comprehensive collection of model galaxies, we generate mock catalog by sampling the parameter space of the disc model in the following fashion:

- M_s is randomly drawn from a uniform logarithmic distribution in the range $9 < \log(M_s) < 11.5$, allowing us to gauge the effectiveness of RPS as a function of mass.
- We assume a gas content which can comprise up to 50 per cent of the total disc mass. Accordingly, f_{gs} is randomly selected from a uniform distribution in the range $[0.05, 1]$.
- We assume a gas distribution which is either identical or extended up to 2.5 times as the stellar distribution. This entails selecting β from a uniform distribution in the range $[0.4, 1]$.
- Bulge-to-Total ratios are in the range $[0, 0.5]$, thus f_{bs} is selected from a uniform distribution in the range $[0, 1]$.
- We allow the bulge scale radius to lie between 25 per cent of R_s to $2R_s$, which is achieved by drawing ξ from a uniform distribution in the range $[0.5, 4]$.

5.2.2 Setting Halo Parameters

The host haloes are initially modeled using the NFW profile (Navarro et al. 1996). The properties of the host haloes of the galaxies are selected at random according to the following prescription

- The virial mass of the host halo is set as a factor of the total stellar mass of the galaxy. For a given stellar mass ($M_s + M_b$), we randomly select the ratio of stellar to dark matter mass based on the relation (and scatter) found in Moster et al. (2010).
- Analysis of N -body simulations yields a power-law relation between M_{vir} and c_v as a function of redshift (Bullock et al. 2001a; Wechsler et al. 2002; Macciò et al. 2008). The concentration parameter c_v is determined according to the relation and scatter between M_{vir} and c_v found in Muñoz-Cuarteras et al. (2011), with the scatter added randomly to the mean relation.

- Several studies and observations (Syer et al. 1999; Bullock et al. 2001b; Macciò et al. 2008) have found that the spin parameter λ' follows a log-normal distribution

$$P(\lambda') = \frac{1}{\lambda' \sqrt{2\pi}\sigma} \exp\left(-\frac{\ln^2(\lambda'/\lambda'_0)}{2\sigma^2}\right), \quad (54)$$

which is independent of halo mass and appears to have a very weak dependence on redshift. We draw the value of the spin parameter of the host halo based on the above distribution with $\lambda'_0 = 0.031$, $\sigma = 0.57$ based on Muñoz-Cuarteras et al. (2011). We limit our sample to haloes with $\lambda > 0.01$ due to numerical convergence considerations. Systems that do not meet this criterion account for ~ 3.5 per cent of the population.

5.2.3 Selecting m_d and j_d

The relationship between j_d , the fraction of total angular momentum found in the disc, and m_d , the fraction of mass in the disc, can be set by physical considerations. It is often assumed that the baryons, who initially share the density distribution and angular momentum of the halo, conserve their specific angular momentum as the disc is formed. This leads to the following relation

$$\frac{J}{M_{\text{vir}}} = \frac{J_d}{M_s + M_g} \Rightarrow m_d = j_d. \quad (55)$$

Mo et al. (1998) find that the above relation succeeds in fitting the sizes of $z = 0$ discs and we adopt this assumption unless noted otherwise⁵. The above relations assume that no angular momentum was transferred to the halo. If the baryons do lose angular momentum to the halo then eq. (55) should be considered as an upper limit.

The value of m_d is set by eq. (53) once the values of M_s, f_{gs} and M_{vir} have been set.

5.2.4 Disc Stability

Since the values of the parameters are selected randomly and independently of each other, the resulting galaxies generated for our catalog may not be dynamically stable. In order to weed out such galaxies we employ the Toomre stability analysis (Toomre 1964; Dekel et al. 2009), in which a thin stellar disc is deemed unstable when the local gravity overcomes the combined stabilizing effects of rotation and pressure due to turbulent or thermal motions. This criterion is expressed by the Toomre Q parameter having a lower value than a stability threshold $Q_c = 1$

$$Q = \frac{\sigma_R \kappa}{3.36 G \Sigma(R)} < 1, \quad (56)$$

where σ_R is the radial velocity dispersion of the stars, κ is the epicyclic frequency and $\Sigma(R)$ is the surface density of the stellar disc.

The parameter σ_R is not defined in our model since we

⁵ In the above, we have assumed the bulge has no angular momentum, and whatever angular momentum lost during the bulge formation was transferred entirely to disc. Relaxing this assumption, namely that the entire baryonic component conserves its specific angular momentum leads to $j_d = m_d + m_b$, with $m_b = M_b/M_{\text{vir}}$.

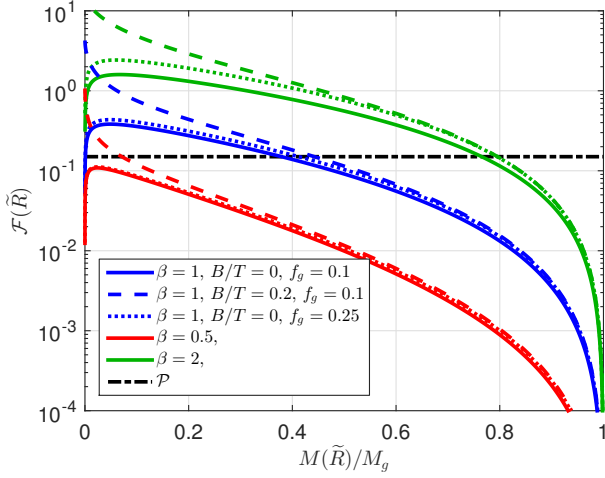


Figure 17. The binding gravitational force in a $M_s = 10^{10} M_\odot$ disc versus the enclosed gas mass for various disc models. Solid lines denote bulge-less disc galaxies of gas fraction $f_{gs} = 0.1$ for $\beta = 1$ (blue), $\beta = 0.5$ (red) and $\beta = 2$ (green). Dashed lines denote galaxies with $B/T = 0.2$, $\xi = 3$ and $f_{gs} = 0.1$ and dotted lines denote bulge-less galaxies of $f_{gs} = 0.25$. The galaxy is embedded in $M = 4.8 \times 10^{11} M_\odot$, $c_v = 10$ NFW dark matter halo. The black horizontal line demarks a value of \mathcal{P} , the L.H.S of the stripping condition eq. (60), which is typical for a satellite at $0.5R_c$ of a $10^{15} M_\odot$ cluster. The intersection point of that line with the \mathcal{F} curves denoting the amount of gas being stripped in each case. As a galaxy moves closer to the cluster centre, the \mathcal{P} line will rise in value. It is clear that varying the gas fraction has little effect on the binding force, and the bulge has a significant effect only in the central areas.

do not account for the orbital properties of the stars but treat the disc as a single entity. To solve this shortcoming, we consider the case of a thick galactic disc. For a stable, relaxed system one may assume that the velocity dispersion components are proportional to each other. Thus $\sigma_R \propto \sigma_z$ where z is the direction perpendicular to the disc plane. By expanding our disc model to account for the disc thickness we can estimate the value of σ_z and by proxy obtain a value for σ_R . We once again turn to the Isothermal sheet model, in which the velocity dispersion in the z direction is related to the velocity dispersion in the x direction by

$$\sigma_z^2(R) = 2\pi G \Sigma(R) z_s. \quad (57)$$

Observations show that the scale height z_s is generally independent of R and, to a good approximation, a constant fraction of the scale radius R_s (van der Kruit & Searle 1981a,b, 1982), such that $z_s = \zeta R_s$. This allows us to randomly select appropriate scale heights for the galaxies based on observed distributions (Bizyaev & Mitronova 2002), and thus determine σ_z .

By further assuming that $\sigma_R \propto \sigma_z$ (Kregel et al. 2005), the Q parameter can be calculated. We discard galaxies for which the value of Q for any point on the disc drops below 1. Using this criteria we find that ~ 1 per cent of the discs generated are unstable. Based on the assumptions detailed above, we have generated a mock catalog of order 1.9×10^4 stable galaxies, which will serve for testing the ram-pressure stripping of galactic gas.

5.3 Employing the Stripping Condition in a NFW Model Cluster

With a catalog of galaxies covering the relevant parameter space in hand we can now assess the effectiveness of RPS on the gas in the galaxy, embodied by eq. (3).

As before, we begin by modeling the ICM with a NFW model (§4.1.2) and assume the galaxy speed is identical to the virial velocity (§4.3.1). Under these assumptions, the ram-pressure, eq. (19) and binding gravitational force eq. (45) can be inserted into the stripping condition eq. (3)

$$\varepsilon f_c \frac{G}{4\pi} \frac{M_{\text{vir}}^2}{R_c^4} \left[\mathcal{A}(1; c_v) \tilde{r} (c_v^{-1} + \tilde{r})^2 \right]^{-1} \geq \pi G \Sigma_s^2 f_{gs} \mathcal{F}(\tilde{R}). \quad (58)$$

For the sake of convenience, we define a new quantity encapsulating the cluster parameters $\Sigma_c \equiv M_{\text{vir}}/(2\pi R_c^2)$. Scaling for typical values we find, making use of eq. (1),

$$\Sigma_c \simeq \begin{cases} 2.4 \times 10^7 \left(\frac{M_{\text{vir}}}{10^{15}} \right)^{\frac{1}{3}} M_\odot \text{ kpc}^{-2} & z = 0 \\ 4.6 \times 10^7 \left(\frac{M_{\text{vir}}}{10^{15}} \right)^{\frac{1}{3}} M_\odot \text{ kpc}^{-2} & z = 0.6 \end{cases}. \quad (59)$$

The stripping condition now takes the form

$$\mathcal{P}(\tilde{r}_p) \equiv \varepsilon \frac{f_c}{f_{gs}} \left(\frac{\Sigma_c}{\Sigma_s} \right)^2 \left[\mathcal{A}(1; c_v) \tilde{r} (c_v^{-1} + \tilde{r})^2 \right]^{-1} \geq \mathcal{F}(\tilde{R}). \quad (60)$$

We recall that $\mathcal{F}(\tilde{R})$ describes how the binding force changes as a function of distance from the galaxy centre. $\mathcal{P}(\tilde{r}_p)$ embodies the strength of the ram-pressure at a given position, normalized to the properties of a specific galaxy. As before, ε is a fudge-factor of order unity which encapsulates any uncertainties in the model.

To find the effect of the ram-pressure we relate the gravitational binding force acting on a gas element at given radius with the gas mass enclosed within that radius. A galaxy at a given position within the cluster will be characterized by a value of \mathcal{P} which can be equated with \mathcal{F} , which in turn determines how much mass is unaffected by the ram-pressure.

In principle, stripping of mass from the galaxy decreases the self-gravity. We ignore this effect since we are only stripping the gas, which accounts for a small contribution to the gravitational force, while the main contributors to the force, the stellar disc and dark matter halo, are unaffected by RPS (and as shown in §4.2, tidal stripping which can affect the stellar and dark matter components is not relevant in the cluster outskirts). We assume the rest of the galaxy is unaffected by the ram-pressure, an assumption which is supported by simulations (Quilis et al. 2000).

In Fig. 17 we show the $\mathcal{F}(\tilde{R}) - M(\tilde{R})$ relation for several illustrative examples of a $M_s = 10^{10} M_\odot$ galaxy with a gas-to-stellar mass ratio of $f_{gs} = 0.1$ embedded in an $M_{\text{vir}} = 4.8 \times 10^{11} M_\odot$, $c_v = 10$ NFW dark matter halo. The different coloured solid lines in the plot correspond to different gas distributions: (a) A distribution identical to the stellar component ($\beta = 1$, blue), (b) A distribution which is twice as extended, ($\beta = 0.5$, red), (c) A distribution which is twice as compact ($\beta = 2$, green), all in a galaxy without a bulge component. Gas rich galaxy models with an enhanced gas fraction of $f_{gs} = 0.25$ are plotted with dotted lines. In addition, galaxy models with a bulge of $B/T = 0.2$ and disc-to-bulge scale radius ratio of $\xi = 3$ (dashed lines), are also shown.

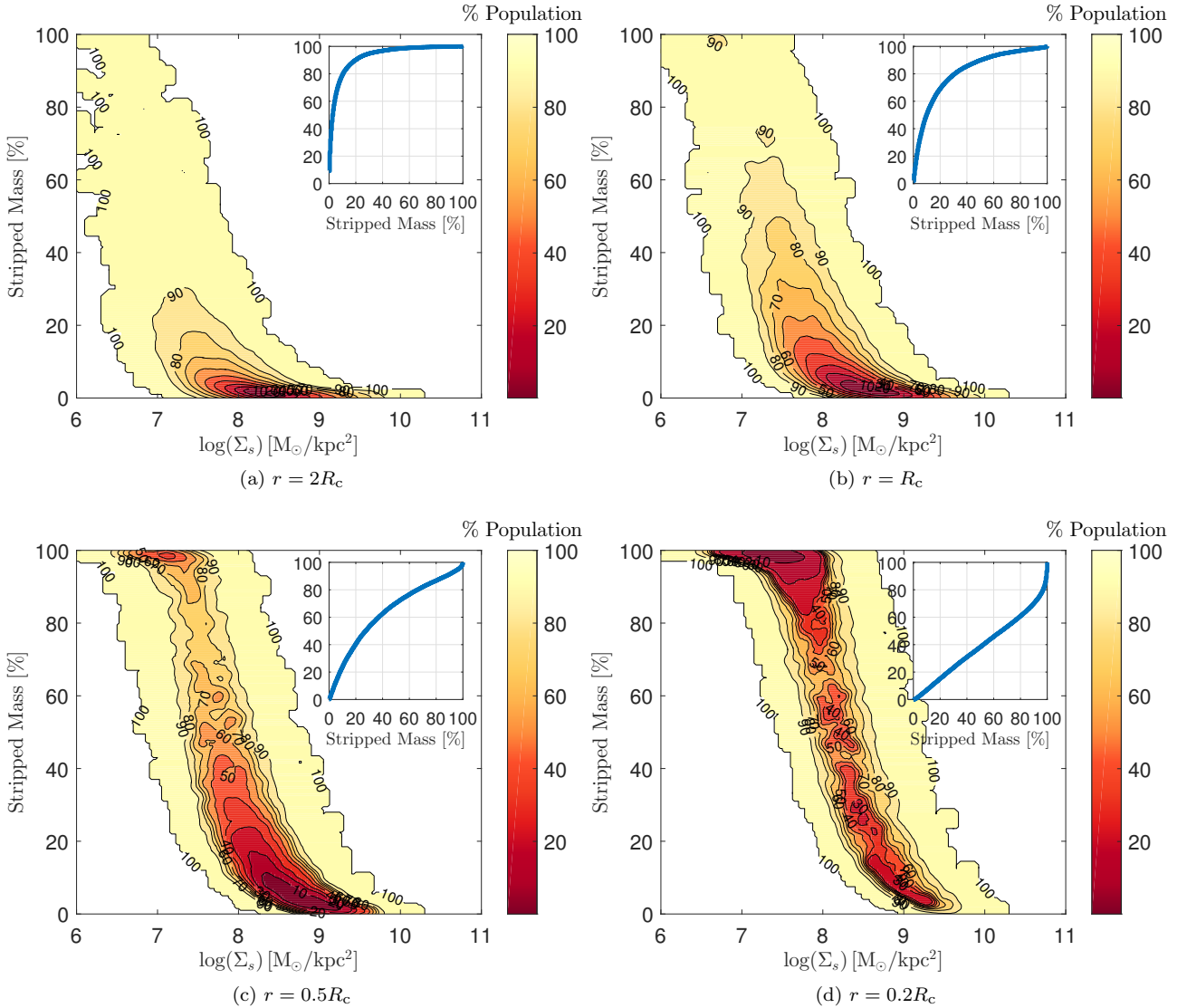


Figure 18. The distribution of satellite galaxies in the mock catalog on a plane relating the parameter Σ_s and the percentage of stripped mass at a given position in a $M_{\text{v,clust}} = 10^{15} M_{\odot}$ NFW cluster and a gas fraction of $f_c = 0.15$. Coloured contours correspond to the percentage of the galaxy population enclosed within the contours. The four panels correspond to the stripping at different positions in the cluster: $2R_c$ (a), R_c (b), $0.5R_c$ (c) and $0.2R_c$ (d). The inlay shows the cumulative distribution of the stripped mass in the catalog galaxies. At $1R_c$ we find that 50 per cent of the population has lost less than 20 per cent of the mass and less than 10 per cent of the galaxies have lost more than 60 per cent of the gas. The stripping can be seen to be ineffective at $1R_c$ and beyond, but within the virial radius a large part of the population has lost a significant amount of gas. The percentage of galaxies who lost more than half their gas is $\lesssim 5$ per cent at $2R_c$, 15 per cent at $1R_c$, 30 per cent at $0.5R_c$ and 60 per cent at $0.2R_c$.

We see in the figure that a value of $\mathcal{P} = 0.15$, typical for a satellite at $0.5R_c$ of a $10^{15} M_{\odot}$ cluster (shown as a horizontal black line), corresponds to a stripping of ~ 20 per cent of the mass for the compact distribution, about 40 per cent in the case of an identical distribution and in the case of an extended gas distribution all of the gas is removed in the bulge-less model, whereas 10 per cent or so of the gas remain if a bulge is present. Thus we can see that the gas distribution is very important in setting the effectiveness of RPS. The bulge can be seen to have a strong influence in the central areas of the galaxy, while increasing the gas fraction in the galaxy does very little to affect the binding force. As a galaxy moves closer to the cluster centre, $\mathcal{P} \propto \tilde{r}_p^{-2}$ increases

and the horizontal line will rise, indicating more stripping of the gas.

In our catalog, we find a mean value⁶ of $\langle \log \Sigma_s \rangle = 10^8$ which means that at the virial radius $r/R_c = 1$, the parameter \mathcal{P} will be of order 0.05 for a typical cluster, using eqs. (59) and (60) (assuming $\varepsilon = 1$). Thus, a galaxy of $M_s = 10^{10} M_{\odot}$, as shown in Fig. 17, will lose at most ~ 50 per cent of its gas if its gas distribution is extended compared to the stars. If the gaseous component is not extended the mass loss will be much smaller. This indicates that RPS is most likely not

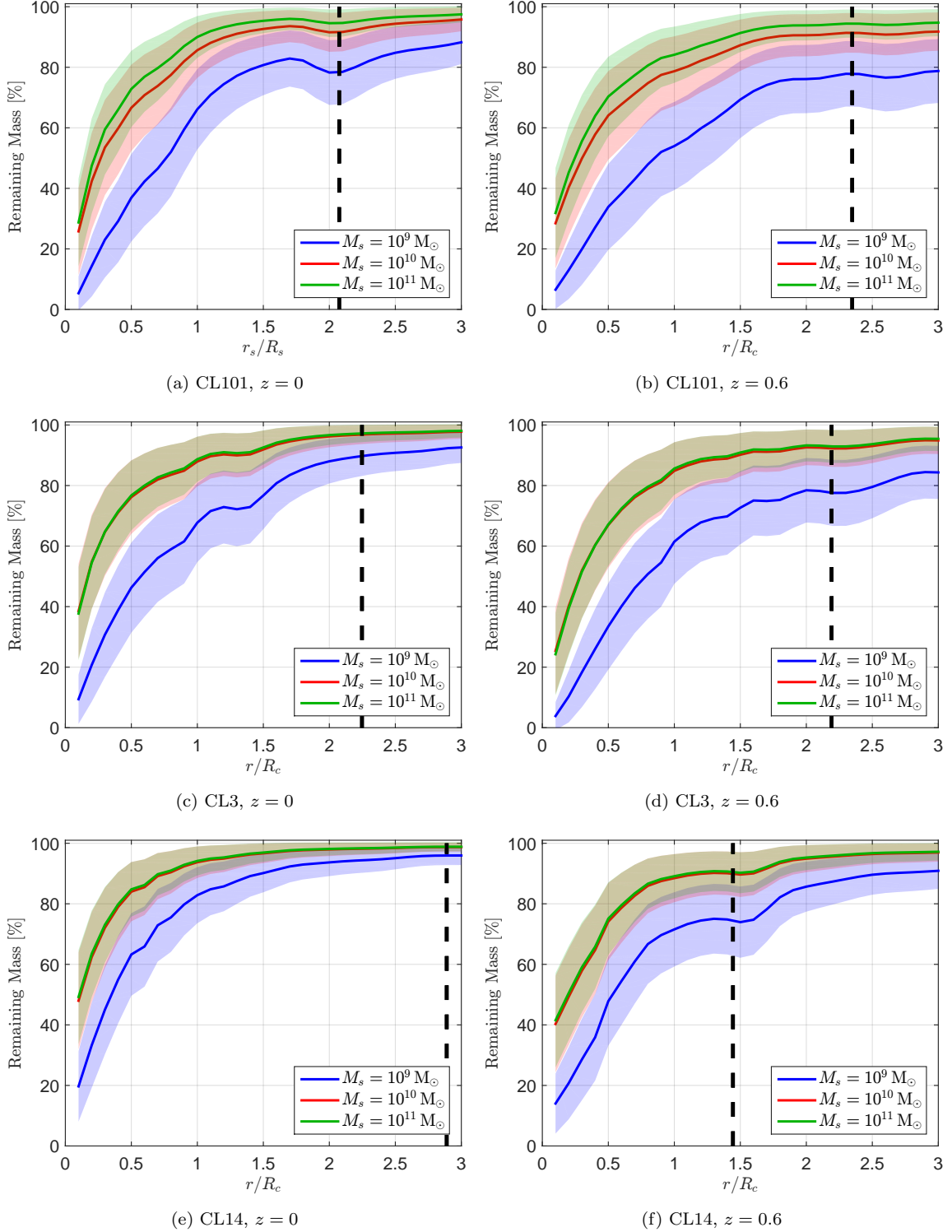


Figure 19. RPS of galaxies in the simulated clusters. The ram-pressure is calculated from the gas density profiles of 3 simulated clusters: CL101 (a) & (b), CL3 (c) & (d) and CL14 (e) & (f), at $z = 0$ (left) and $z = 0.6$ (right). Mass stripping is calculated for three mock catalogs of 1000 galaxies each for which the stellar disc mass is constant: $10^9 M_\odot$ (blue), $10^{10} M_\odot$ (red) and $10^{11} M_\odot$ (green). The mean value of the remaining gas mass for each of the catalogs is shown (solid line) with the shaded region corresponding to a range of 1σ about the mean. Also shown is the minimal location of the shock edge as defined in §3.2 (black dashed). The value of the fudge-factor for RPS is $\varepsilon = 1$. We find that the stripping becomes pronounced within the virial radius of the cluster. Beyond the virial radius, satellites of $M_s > 10^{10} M_\odot$ undergo very little stripping while the low-mass satellites still retain more than 60 per cent of their gas mass. Satellites in higher mass clusters naturally experience more stripping.

effective in removing the gas from galaxies when they are beyond the virial radius of clusters.

We examine the stripping for the entire galaxy catalog in Fig. 18, where the galaxies are assumed to be in a NFW model $10^{15} M_{\odot}$ cluster with a gas fraction of $f_c = 0.15$, assuming $\varepsilon = 1$. We find the amount of stripped mass in each galaxy and show the distribution of the galaxy population according to the stripped mass and Σ_s for 4 different positions within the cluster: $2R_c$, $1R_c$, $0.5R_c$ and $0.2R_c$. The contours correspond to the percentage of the population enclosed within them, and the cumulative distribution of the stripped mass is also shown in the inset.

At twice the virial radius (Fig. 18a) the stripping is practically negligible, with 50 per cent of the population retaining more than 95 per cent of their gas, and 90 per cent of the population retaining more than 65 per cent of their gas. At the virial radius (Fig. 18b), the stripping is still largely ineffective, with about 80 per cent of the galaxies retaining more than 60 per cent of their gas, although there are already some galaxies (~ 3 per cent) who have been stripped of more than 90 per cent of their gas. These levels of stripping were achieved with the assumption of maximal RPS effectiveness $\varepsilon = 1$.

Within the virial radius (Figs. 18c and 18d), RPS becomes an important process, affecting nearly all the galaxies to some extent. In the central regions ($\sim 0.2R_c$) over half of the galaxies have lost more than 60 per cent of their gas, and of these most of lost virtually all their gas.

5.4 RPS of the Galactic Disc in Simulated Clusters

We examine the effectiveness of the stripping in a more realistic setting in Fig. 19 by using the gas density profiles from 3 of our simulated clusters: CL101, CL3 and CL14 at $z = 0$ and $z = 0.6$, in a similar fashion to Fig. 12. As before, the ram-pressure is calculated based on the gas density profile and under the assumption that the speed of the galaxy is equal to the virial velocity of the cluster. The fudge factor ε is also employed to account for uncertainties in the model, and is set to $\varepsilon = 1$ to ensure maximal stripping.

As test cases we generated mock catalogs of 1000 galaxies each, in which the stellar disc mass was identical for all galaxies. Three such catalogs were generated with stellar disc masses of 10^9 , 10^{10} and $10^{11} M_{\odot}$.

As one would expect, galaxies travelling in clusters of higher mass experience more stripping. One can also see that galaxies of lower masses are more susceptible to RPS. Here too the RPS becomes effective when galaxies are within the virial radius of the cluster. As noted in relation to Fig. 13, while the stripping may seem more effective at $z = 0.6$, one must bear in mind that the virial radius at $z = 0.6$ is lower by a factor of ~ 2 . In essence, one is examining stripping at a much smaller radius in comparison to the $z = 0$ case, since the cluster gas density profile does not change significantly between these times at a given position.

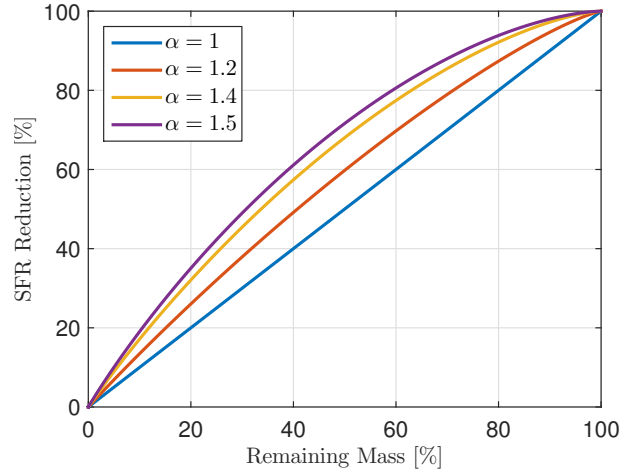


Figure 20. The relation between the remaining gas mass in a galaxy and the reduction in SFR as a result of the mass loss. The different lines correspond to different values of α , the exponent in the Kennicutt–Schmidt law $\Sigma_{\text{SFR}} \propto \Sigma_{\text{gas}}^{\alpha}$. The SFR of a galaxy with only 40 per cent of its gas remaining will be ~ 60 per cent of its original value, for values of $\alpha \simeq 1.4$. To reduce the SFR of a galaxy to half its initial value one must remove at least 70 per cent of the gas.

5.5 Relating the Mass Stripping to Star Formation Quenching

In the previous sections we explored the amount of gas removed from the disc of satellite galaxies as a result of RPS. Clearly, removal of the gas from the galaxy should result in a drop in the star formation, but the relation between the two is not necessarily linear.

The observational Kennicutt–Schmidt relation (Schmidt 1959; Kennicutt 1998) relates the surface density of the gas in a galaxy with the star formation rate per unit area, $\Sigma_{\text{SFR}} \propto \Sigma_{\text{gas}}^{\alpha}$, with an exponent in the range of $\alpha = 1 - 1.5$. This relation is seen to hold locally within a galaxy, as well as on average over the entire disc.

Thus, the central areas where the density is higher (and the gravitational binding is stronger) will account for a larger part of the star formation than the outskirts of the disc, even though they contain more mass. RPS, on the other hand, preferentially removes gas from the outskirts. As a result, removing half the gas in the galaxy will not result in a 50 per cent drop in star formation, but rather in a smaller reduction.

For the exponential disc model we employed in this paper (see §5.1.2) one can approximate the SFR using the Kennicutt–Schmidt law for a given galaxy model. For a galaxy which has undergone stripping, one can relate the amount of gas remaining in the galaxy to the reduction in the total SFR, compared to its value before the stripping took place.

In Fig. 20 we show this relation for several representative values of α , the exponent in the Kennicutt–Schmidt law. We see that for $\alpha = 1$, the fraction of remaining mass is equivalent to the reduction in SFR. For $\alpha > 1$, the reduction in SFR will always be smaller than the reduction in mass. The SFR of a galaxy stripped of half its gas will be ~ 70 per cent of its original value for $\alpha \simeq 1.4$. Conversely, to reduce

⁶ The distribution of Σ_s values in our catalog is Gaussian in $\log(\Sigma_s)$ with a mean value of 8.03 and $\sigma = 0.57$.

the SFR of a galaxy to half its original value, one must strip roughly 70 per cent of its gas.

This means that the results for the stripped mass in galaxies shown in Figs. 18 and 19 should be considered as upper-limits to the amount of star-formation quenching in those galaxies. This only enhances the conclusion that RPS is not an effective mechanism for inducing star formation quenching in the outskirts of clusters.

6 STAR FORMATION QUENCHING

The quenching of star formation in galaxies can be achieved by removing enough gas from the galaxy such that there is insufficient fuel for forming new stars. It is common to distinguish between two modes of quenching. If the gas is removed from the galaxy itself, new stars cannot be formed and the shut-down of star formation is very rapid. However, if the gas in the galaxy remains intact, and only the gas from the surrounding halo is removed, star formation can still continue within the galaxy for some time before exhausting the gas in the disc. Since the gas in the disc cannot be replenished the star formation in the galaxy will eventually cease, albeit much more slowly. This is often referred to as quenching by ‘starvation’.

In §4 and §5 we presented two toy models which allowed us to assess the effectiveness of removing the gas, via RPS, from the gas haloes surrounding satellite galaxies as well as from the within the galaxy itself. The two main results of these toy models with respect to star formation quenching in the cluster outskirts ($r \gtrsim R_{\text{vir}}$) are that RPS is *not* effective at removing the gas from within the galactic disc in these regions and thus, rapid quenching cannot take place in the outskirts (assuming no other quenching processes take place) and that RPS is *very* effective in stripping the halo gas surrounding galaxies, even well beyond the virial radius of clusters.

We therefore find that star formation quenching in the outer regions can occur by ‘starvation’—the removal of the gas reservoir in the halo and subsequent decline of star formation over time as the gas within the galaxy is depleted. In contrast, within the virial radius and especially in the inner regions of clusters, ram-pressure can lead to the complete removal of gas from the galaxy leading to very rapid quenching.

In light of these results we wish to determine whether galaxies, after crossing the accretion shock at the edge of the system and losing their gas reservoir will be quenched by the time they reach the virial radius. To do so we must compare the time it takes a satellite to travel from the accretion shock to the virial radius t_{travel} , to the depletion time, the time it takes to use up all the gas within a galaxy t_{depl} .

6.1 Travel Time

As we have seen in §3.2, the shock front demarking the edge of the ICM is typically found at $\gtrsim 2R_{\text{vir}}$. As a first approximation, we assume galaxies travel at the virial velocity and find the time it takes to travel from $2R_{\text{vir}}$ to $1R_{\text{vir}}$, based on

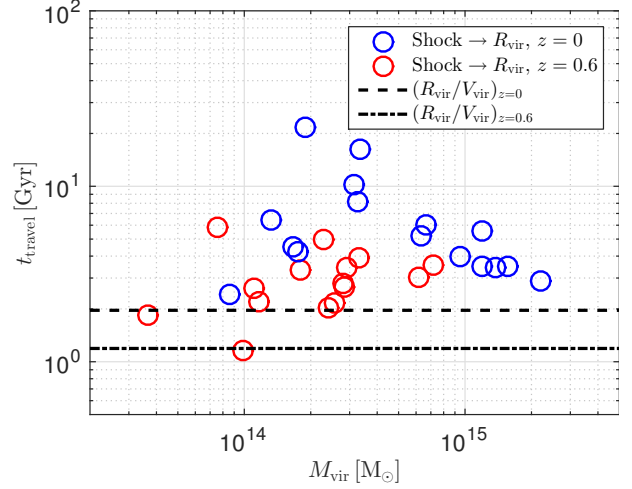


Figure 21. Time of travel for a satellite galaxy, t_{travel} , from $R_{\text{shock}} \rightarrow R_{\text{vir}}$ in the suite of simulated clusters is shown for $z = 0$ (blue) and $z = 0.6$ (red). The values for $t_{2 \rightarrow 1 R_{\text{vir}}}$ at $z = 0$ and $z = 0.6$ are also shown (dashed and dot-dashed, respectively).

the virial relation eq. (1)

$$t_{\text{travel, vir}} = \frac{R_{\text{vir}}}{V_{\text{vir}}} = \frac{R_{\text{vir}}}{\sqrt{GM_{\text{vir}}/R_{\text{vir}}}} = 1.96 \left(\frac{\Delta_{\text{vir}}(z)}{337} \frac{\rho_{\text{ref}}(z)}{\rho_{\text{mean}}(0)} \right)^{-\frac{1}{2}} \text{ Gyr}. \quad (61)$$

This results in a time-scale which, at any given time, is independent of the virial parameters of the system. At $z = 0.6$ we find $t_{2 \rightarrow 1 R_{\text{vir}}} = 1.2 \text{ Gyr}$.

For a more detailed result we turn to our suite of simulated clusters. To assess the typical velocity of incoming objects we created a mass-weighted inflowing radial velocity profile by averaging only over simulation cells in which the radial velocity of the gas is inflowing, i.e. $v_r < 0$,

$$\langle v_r \rangle = \frac{\iint v_r(r, \theta, \varphi) W(r, \theta, \varphi) d\theta d\varphi}{\iint W(r, \theta, \varphi) d\theta d\varphi}, \quad (62)$$

where

$$W(r, \theta, \varphi) = \begin{cases} \rho(r, \theta, \varphi) & v_r < 0 \\ 0 & v_r \geq 0 \end{cases}. \quad (63)$$

The travel time can now be calculated

$$t_{\text{travel}} = \int_{R_{\text{out}}}^{R_{\text{in}}} \frac{dr}{\langle v_r \rangle}. \quad (64)$$

In Fig. 21 we show the calculated travel times for travelling from the shock edge (lowest value, see §3.2) to $1R_{\text{vir}}$, for the clusters at $z = 0$ and $z = 0.6$. As can be seen, the results are of order several giga years and greater than the virial approximation $t_{2 \rightarrow 1 R_{\text{vir}}}$ by a factor of a few.

6.2 Gas Depletion Time

To find the gas depletion time we use the Kennicutt–Schmidt law

$$\bar{\Sigma}_{\text{SFR}} = A \left(\frac{\bar{\Sigma}_{\text{gas}}}{\text{M}_{\odot} \text{ pc}^{-2}} \right)^{\alpha} \quad (65)$$

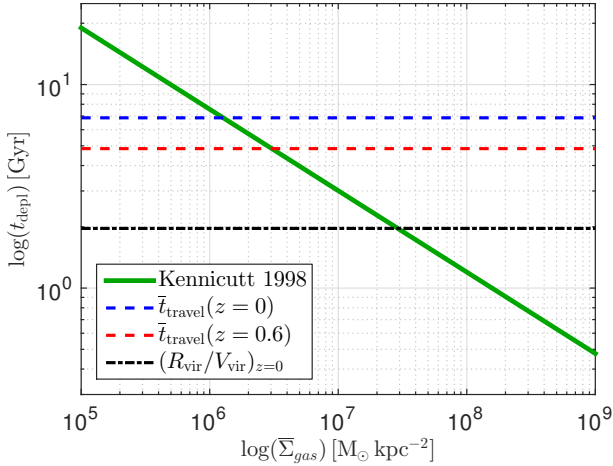


Figure 22. The depletion time inferred from the Kennicutt–Schmidt law as a function of average gas surface density (green). Also shown are the median value for the distribution of travel times in the simulated clusters at $z = 0$ and $z = 0.6$ (blue & red, respectively) as shown in Fig. 21, as well as $t_{2 \rightarrow 1R_{\text{vir}}}$ (black). The depletion times for typical galaxies are of the order of the travel times showing that galaxies may quench by ‘starvation’ even before reaching the virial radius of the cluster.

for the average surface densities of the gas and SFR. Kennicutt (1998) found this relation to hold over several orders of magnitudes in surface density and found the values of the parameters based on observations to be $\alpha = 1.4 \pm 0.15$ and $A = (2.5 \pm 0.7) \times 10^{-4} \text{ M}_{\odot} \text{ kpc}^{-2} \text{ yr}^{-1}$. Additional studies (e.g. Kennicutt et al. 2007; Leroy et al. 2008; Tacconi et al. 2013) found different values for the exponent in the range $\alpha = 1.0\text{--}1.5$, and also found that the relation holds over a large range of redshifts (Tacconi et al. 2013). The relation is also seen to apply locally within a single galaxy, although the parameters of the relation usually vary between different galaxies (Bigiel et al. 2008).

The relation can be theoretically motivated if one assumes that $\text{SFR} \propto \rho_{\text{gas}}/\tau$, where τ is a relevant time scale. If τ is taken to be the free-fall time $t_{\text{ff}} \propto \rho_{\text{gas}}^{-1/2}$ we naturally arrive at the Kennicutt–Schmidt law with an exponent of $\alpha = 1.5$ (Madore 1977). More detailed analysis derived the relation from the physics of molecular clouds, where the actual star-formation occurs (Krumholz & McKee 2005), or by the properties of the density distribution function of the ISM (Kravtsov 2003).

Gas can be depleted either through star formation, or through feedback process, such as supernova feedback or radiative feedback from massive main-sequence stars, which drive outflows from the galaxies. These processes can be assumed to scale with the star formation rate such that $\dot{\Sigma}_{\text{outflow}} = \tau \dot{\Sigma}_{\text{SFR}}$ where $\tau \approx 1$ (Dekel & Mandelker 2014). The average gas density then follows the equation

$$\dot{\Sigma}_{\text{gas}} = -\dot{\Sigma}_{\text{SFR}}(1 + \tau) = -\tilde{A}(1 + \tau)\tilde{\Sigma}_{\text{gas}}^{\alpha}, \quad (66)$$

where $\tilde{A} \equiv A/10^{6\alpha}$ due to unit conversion. The solution to

this equation is ⁷

$$\bar{\Sigma}_{\text{gas}}(t) = \left(\bar{\Sigma}_0^{1-\alpha} + (\alpha - 1)(1 + \tau)\tilde{A}t \right)^{\frac{1}{1-\alpha}}, \quad (67)$$

where $\bar{\Sigma}_0 \equiv \bar{\Sigma}_{\text{gas}}|_{t=0}$. As one would expect, the gas surface density goes to 0 asymptotically.

We define the depletion time as the time in which the average surface density drops to a given fractional value ϵ

$$t_{\text{depl}} = (\epsilon^{1-\alpha} - 1) \frac{\bar{\Sigma}_0^{1-\alpha}}{(\alpha - 1)(1 + \tau)\tilde{A}} \\ = 3.01 \left(\frac{\bar{\Sigma}_{\text{gas}}}{10^7 \text{ M}_{\odot} \text{ kpc}^{-2}} \right)^{-0.4} \text{ Gyr}. \quad (68)$$

The typical depletion value given above is defined for representative values of $\epsilon = 0.1$ and $\alpha = 1.4$, $\tilde{A} = 10^{-14}$ and is consistent with observations (Kong 2004; Bigiel et al. 2008; Leroy et al. 2008; Pflamm-Altenburg & Kroupa 2009; Bauermeister et al. 2013).

In Fig. 22 we show the depletion time as a function of $\bar{\Sigma}_{\text{gas}}$ as well as the median of the travel time distribution in our simulated clusters. As can be seen, the depletion time and travel times are of the same order for ordinary disc galaxies ($\bar{\Sigma}_{\text{gas}} \sim 10^6\text{--}10^7 \text{ M}_{\odot} \text{ kpc}^{-2}$).

The values of t_{depl} found above should be treated as an upper limit to the star formation quenching time. Observations and theoretical studies point to a threshold gas density necessary for star formation (Krumholz et al. 2009). This threshold may be reached before the gas is completely depleted. Another factor to consider is that the ram-pressure exerted by the ICM can also enhance the star formation rate of a satellite galaxy due to the additional pressure exerted on the ISM of the satellite galaxy (Bekki & Couch 2003; Kronberger et al. 2008). If so, the actual depletion time may be even shorter.

We see therefore that the depletion time (and by extension the star formation quenching time) and the travel time are of the same order and that galaxies beyond the virial radius in clusters may quench due to gas depletion in the galaxy after the loss of their halo gas reservoir to RPS, even before crossing the virial radius for the first time.

While we have shown that quenching via ‘starvation’ is feasible for galaxies beyond the virial radius of the cluster, we note that not all galaxies will necessarily be quenched. As seen in Fig. 21, the typical travelling time varies between clusters, and galaxies with long depletion times may reach the virial radius before quenching if the travel time is sufficiently low. This can account for the observed star-forming galaxies found within the virial radius.

7 DISCUSSION: VALIDITY OF THE RPS MODEL

Of the various processes occurring in the extended ICM which can lead to gas depletion and star formation shut-down we focus here on ram-pressure stripping. This hydrodynamic process is known to occur in clusters (Cayatte et al.

⁷ In the case of $\alpha = 1$, the solution to eq. (66) is an exponential decay with a decay time-scale of $(\tilde{A}(1 + \tau))^{-1}$.

1994; Kenney et al. 2014; Abramson & Kenney 2014) and has been studied analytically (Gunn & Gott 1972; Gisler 1976) and numerically (Gisler 1976; Abadi et al. 1999, also see Roediger 2009 and references therein).

To study the effectiveness of RPS we employed a simple analytic toy-model which we apply to stripping of the hot halo gas surrounding satellite galaxies and to the stripping of gas within the galactic disc itself. Our model, while easy to implement, is based on a set of simplifying assumptions. The model is instantaneous rather than dynamical—we assess the mass loss for a given halo/galaxy at a given position in the cluster while disregarding its history and ignoring the subsequent evolution. We assume mass loss occurs rapidly and do not address the dynamical response of the system to the mass loss (Smith et al. 2012).

In modelling the gas distribution of the gas halo of the satellites, we have assumed that the gas is isothermal and in hydrostatic equilibrium within the dark matter potential. Gas distributions which assume a more general polytropic equation of state for the gas have been suggested (e.g. Komatsu & Seljak 2001), and we intend to extend our RPS model to include these profiles in a future work. In addition, we are ignoring the multiphase nature of the gas in the disc, an omission which over-estimates the ability of RPS to remove the clumpy cold gas component (Tonnesen & Bryan 2009).

In reality, studies have shown that the gas removal from a galaxy undergoing stripping is a multi-stage process in which the gas located beyond the stripping radius is first displaced from the disc over a time-scale of ~ 10 Myr and is subsequently completely unbound over longer time-scales of ~ 100 Myr (Schulz & Struck 2001; Marcolini et al. 2003; Roediger & Hensler 2005; Roediger & Brüggen 2007). In the interim, some of the displaced gas can be re-accreted to the galaxy. A third phase of prolonged viscous stripping (Nulsen 1982) follows.

Despite the inaccuracies of the simple model employed in this paper, we find it is a very useful tool whose results regarding the stripping in the cluster outskirts can be trusted, if wielded properly. In both the halo gas and disc gas stripping scenarios we used the model to obtain a lower or upper limit for the stripping effectiveness to overcome the shortcomings of the model.

In the halo gas stripping scenario we found that the stripping was very effective for typical satellite masses even when the effect of RPS was reduced by hand (via the fudge-factor ε' , Fig. 11). Since RPS only affects the gas and not the dark matter in the cluster outskirts (§4.2) the potential well of the satellite will remain largely unchanged, and since the RPS is so strong, the assumption of rapid gas removal is justified.

Due to the shortcomings of the model which we listed above, one may argue that for the scenario of stripping gas from the disc, the model over-estimates the stripping by assuming rapid and total gas removal. However, we find that the stripping is largely ineffective, even when ensuring a maximal effect of the ram-pressure. This is done by assuming a relatively high cluster mass ($10^{15} M_{\odot}$) and taking a maximal value of the fudge-factor $\varepsilon = 1$. We can thus be assured that in the outskirts of clusters RPS is not an effective form of disc gas stripping.

In focusing on RPS we have also neglected other pro-

cesses which may lead to gas depletion. Two relevant dynamical processes are tidal stripping by the cluster and interactions with other satellites in close encounters, the combined effect of which is known as ‘galaxy harassment’ (Moore et al. 1996). Tidal stripping is strongly dependent on the cluster-centric distance (Dekel et al. 2003) and as shown in §4.2, can be ignored in the outskirts of clusters (see also the Appendix of McCarthy et al. 2008). Due to the high relative velocities between satellite galaxies, perturbations induced by close encounters are expected to be small (Boselli et al. 2006).

Two additional relevant *hydrodynamical* processes are viscous stripping (Nulsen 1982) and thermal evaporation (Cowie & Songaila 1977). Viscous stripping occurs when the gas in the outer layers of a galaxy travelling through the ICM experiences a momentum transfer due to viscosity which can lead to gas removal. The effectiveness of the stripping depends on whether the flux is laminar or turbulent, which in turn depends on the size of the galaxy. Thermal evaporation occurs at the interface between the hot ICM and the much cooler ISM. The mass loss rate is sensitive to the temperature of the ICM $\dot{M} \propto T_{\text{ICM}}^{3/2}$, and the presence of magnetic fields which can reduce the efficiency of this process.

The effect of these two processes on the disc are qualitatively similar to that of RPS, in that only the gas in the satellite (and not the stellar or dark matter components) is affected and the processes work on gas from the outside in. In terms of relative importance, in the central regions of clusters both RPS and viscous stripping are expected to be the dominant mass loss channels in galaxies which are extended and/or characterized by high orbital velocities, while thermal evaporation becomes important for smaller (dwarf) galaxies (Boselli et al. 2006). Roediger & Brüggen (2008) and Roediger (2009) find that viscous stripping has a minor effect compared with RPS and its impact is felt only over much longer time-scales.

While thermal evaporation has been shown to be equally as important as RPS in the central regions of cluster (Nulsen 1982), since it is strongly dependent on the temperature, its effect is greatly reduced in the outskirts of clusters. As seen in Fig. 5, the temperature in the outskirts can drop to as much as 20 per cent of the temperature within R_{vir} which entails a mass loss rate due to evaporation which is 90 per cent smaller than in the central regions of the cluster.

Another aspect of the interaction we have neglected is the effect of magnetic fields on the mass loss due to RPS. Interactions between the magnetic fields of the ISM and ICM may somewhat suppress mass loss, depending on the orientation of the ICM magnetic field to the direction of motion of the galaxy, with a parallel orientation leading to stronger suppression of mass loss. The overall effect however is found to be mild (Shin & Ruszkowski 2014; Tonnesen & Stone 2014; Ruszkowski et al. 2014).

For the case of halo gas stripping, one must consider the confining effect produced by the ICM pressure. The ICM pressure may lead to a contraction of the gas halo and reduce the efficiency of RPS. Bahé et al. (2012) find that the ram-pressure is generally dominant over confinement pressure.

8 CONCLUSION AND DISCUSSION

It is common practice to treat the virial radius, defined by the mean overdensity of the dark matter halo with respect to the mean cosmological density, as the outer edge of a collapsed cosmological object. Although this definition is physically motivated by the process of energy-conserving virialization (embodied in the spherical collapse ‘Top Hat’ model), in the case of cluster-sized systems $\gtrsim 10^{14} M_{\odot}$ the true extent of the cluster hot gas is far greater.

We examined 16 high-resolution simulated cluster systems and found that, at least from $z = 0.6$ and onwards, the virial accretion shock extends to well beyond the virial radius and is usually found at a distance of $\sim 2.5 R_{\text{vir}}$, an estimate based on the peak of the entropy profile of the cluster and the maximal negative entropy gradient along the profile.

The virial accretion shock is comprised of several shock fronts (‘lobes’) which extend between the large scale filaments and merge seamlessly with the cylindrical shocks surrounding the filaments that feed the cluster. Though very rough, our edge detection method manages to capture the main features of the shock edge, and gives a reliable estimate for the shock edge fronts in the simulated clusters.

The relative positions of the accretion shock and R_{vir} show that the standard virial radius encloses $\lesssim 10$ per cent of the ICM volume. R_{vir} should be treated as a useful ball-park scale of the cluster size, but not necessarily its edge. As a result it should come as no surprise that galaxies at cluster-centric distances of several times R_{vir} are affected by the cluster environment (Park & Hwang 2009).

Lau et al. (2015) have shown that the profiles of cluster properties are self-similar if normalized by the mass accretion rate into the cluster. As a result, they find that the location of the accretion shock, when cast in units of R_{200} , is strongly dependent on the mass accretion parameter. Clusters with a high accretion rates have smaller accretion shocks. We have confirmed this behavior in our simulated cluster suite as well.

Another measure of the ‘edge’ of a dark matter halo is the ‘splashback’ radius (Diemer & Kravtsov 2014; Adhikari et al. 2014) which is defined by a sharp drop in the density profile of the halo. More et al. 2015 find that the splashback radius is typically larger than the virial radius in high mass halos, in general agreement with our findings.

Observational confirmation of the shock location should be possible. The virial shock front can accelerate charged particles to very high energies of $\gtrsim \text{TeV}$ which then Compton-scatter CMB photons into γ -rays (Loeb & Waxman 2000; Keshet et al. 2003). The γ -ray signal should be accompanied by a signal in hard X -rays (Kushnir & Waxman 2010) and a synchrotron emission (Loeb & Waxman 2000; Keshet et al. 2004), which may be detected in radio observations. The resultant signal is expected to resemble an elongated ring due to the filamentary structure surrounding the cluster (see §3.1).

Keshet et al. (2012) have reported the discovery of an elongated γ -ray ring structure surrounding the Coma cluster at a radius of $\sim 5 \text{ Mpc}$ which they argue is a signal of the virial accretion shock. The virial radius of the Coma cluster is $R_{200} \simeq 2.3 \text{ Mpc}$, so that the shock signal is detected at $\sim 2 R_{200}$, in complete agreement with our findings. We expect that future observations will discover more evidence

of the existence and position of the virial accretion shock surrounding clusters.

Having established that the environment of the cluster extends out to $\sim (2-3) R_{\text{vir}}$ we examined how the extended environment can affect satellite galaxies in the outskirts of the cluster. To that end we employed simple analytic models to gauge the effect of RPS both on the gas within a satellite galaxy as well as the gas in the halo that surrounds it, and extended the analysis by examining the RPS expected on analytic galaxy models within our simulated cluster suite.

The results of our RPS models lead us to the following conclusions in terms of gas depletion and star formation quenching

- a) RPS in the outer regions of clusters, especially high-mass clusters, is very effective in removing the halo gas surrounding individual galaxies, between 40 and 70 per cent at $2 R_{\text{vir}}$. When the satellites reach R_{vir} less than 30 per cent of the gas remains in high-mass satellites, with low-mass satellites retaining less than 10 per cent of their initial gas halos.
- b) RPS is *not* an effective channel for removing the gas from within galactic discs in the outskirts of clusters.
- c) Once a satellite crosses R_{vir} and as it falls towards the centre of the cluster, RPS becomes an increasingly important mechanism for removing gas from the galaxy proper.

We address here quenching of satellite galaxies by the ICM of a host cluster in the regions of $\gtrsim 1 R_{\text{vir}}$. The quenching scenario we envision is that of ‘starvation’ – the gas in the galaxy is depleted from the galaxy via star formation and feedback processes over a time-scale of several giga years and no new gas can be accreted from the local gas reservoir since it has been removed by RPS. The gas cannot be replenished from the hot ICM since its cooling time is very long and the typical satellite velocity is higher than the escape velocity of the satellite.

Once the gas density in the galaxy drops below a critical threshold, star formation is quenched abruptly. This is consistent with the ‘delayed-then-rapid’ quenching scenario inferred by recent studies (Trinh et al. 2013; Mok et al. 2013; Wetzel et al. 2013), as well as the findings of Tal et al. (2014) that the onset of quenching in satellites in galaxy groups is delayed in comparison with the quenching of the central galaxy (see also Woo et al. 2015).

By comparing the typical times, i.e. the time it takes a galaxy to traverse the distance from the accretion shock to R_{vir} (‘travel time’), and the gas depletion times we find that it is quite plausible for a galaxy reaching the virial radius of the cluster for the first time to be quenched due to ‘starvation’. This provides a natural explanation for the quenched population of galaxies, and especially disc galaxies, found in the outskirts of clusters (Park & Hwang 2009).

The scenario of satellite quenching in the environment of the cluster which extends to $\sim (2-3) R_{\text{vir}}$ is consistent with the observed ‘galactic conformity’, i.e. large scale correlations between quenched satellites and quenched centrals over large distance scales of several Mpc (Weinmann et al. 2006; Ann et al. 2008; Kauffmann et al. 2010).

The ‘starvation’ quenching mode has been considered before (Larson et al. 1980; Balogh et al. 2000; McCarthy et al. 2008; Bekki 2009) but usually under the assumption that the virial radius marked the edge of the system. As a result, the time-scales involved led to the conclusion that

the process was not fast enough and that to match the observations of the quenched population, galaxies must have been quenched in the centres of smaller groups before becoming part of the cluster, a scenario known as ‘pre-processing’ (Balogh et al. 2000; Jaffé et al. 2012; Wetzel et al. 2013; Fang et al. 2016). However, if the edge of the ICM is much more extended and the gas reservoir in the haloes of individual galaxies is removed much earlier, one need not invoke ‘pre-processed’ or ‘splashback’ galaxies (Wetzel et al. 2014) to account for the quenched population in clusters.

Bahé et al. (2013) reached a similar conclusion based on the results of SPH simulations of satellites in clusters (see also Cen 2014; Jaffé et al. 2015). In this paper we have presented a more comprehensive analytic framework to explore the RPS of the halo gas and the gas within the galaxy. By making use of an analytic modeling of the satellite galaxies we are in full control of the parameters and attributes of the galaxies. This allows us to gauge the effectiveness of RPS on a wide range of galaxy types, beyond those which are reliably produced in a simulation, resulting in a better understanding of what makes a galaxy more (or less) susceptible to stripping. The model afforded the chance to explore the effectiveness of RPS over a large and exhaustive parameter space thus enabling a mapping of the limits of RPS as a quenching mechanism in satellite galaxies.

The ram-pressure which acts to remove the gas halo reservoir of the galaxy may also affect the depletion time indirectly by enhancing the star formation rate due to the additional pressure exerted on the ISM. Evidence for this has been seen in numerical studies by Bekki & Couch (2003); Kronberger et al. (2008); Kapferer et al. (2008, 2009). Tonnesen & Bryan (2012) however find no signs of star formation enhancement, perhaps due to differences in the numerical scheme.

We note that star formation quenching may occur before the typical depletion time has passed due to other processes which lead to more rapid quenching. One such example is the ‘morphological quenching’ – the gas depletion leads to a drop in surface density of the gaseous disc leading to an increased disc stability, eq. (56), which may lead to a shut-down of star formation (Martig et al. 2009, 2013). Another example is the compaction of the gas in the disc which leads to increased star formation and quenching (Zolotov et al. 2015).

Though we show that by removing the halo gas surrounding a galaxy, star formation quenching via ‘starvation’ can occur, it must be stressed that not all the satellites will necessarily be quenched completely, and indeed star forming galaxies are regularly observed within clusters. In addition, Sun et al. (2007) and Jeltama et al. (2008) find evidence of gas haloes surrounding satellite galaxies in the central regions of clusters demonstrating that not all satellites are stripped of their halo gas.

As we have pointed out in Zinger et al. (2016), gas streams in clusters can penetrate into the very centre of the cluster (e.g. see Fig. 14). Satellites which travel along the inflowing streams may suffer very little stripping, if they are co-flowing with the surrounding medium, and hypothetically could reach the centre of the cluster with their gas content intact. Conversely, if the gas in the filaments is hot enough, as shown in Zinger et al. (2016), the galaxies in the filaments may not be able to accrete new gas and quench

by ‘starvation’, albeit over longer timescales, once the gas in the galaxy and in the gaseous halo has been depleted. Further study is needed to confirm the validity of this scenario and implications.

In addition, as seen in Fig. 22 galaxies with sufficiently long depletion times may reach R_{vir} before being quenched. Since the typical travel times for reaching R_{vir} vary between different clusters (Fig. 21), one may expect to find clusters in which star-forming galaxies can be found even well within the virial radius.

In this paper we have explored in depth one aspect of the environmental effect of the ICM on satellite galaxies found beyond the virial radius, namely RPS. The understanding that the cluster influence extends out to distances of several mega-parsecs should prompt further observational, theoretical and numerical studies of the ways the ICM affects galaxies in these regions.

ACKNOWLEDGEMENTS

We acknowledge stimulating discussions with Yuval Birnboim, Joanna Woo and Sandro Tacchella. This work was supported by ISF grant 24/12, by GIF grant G-1052-104.7/2009, by a DIP grant, by the I-CORE Program of the PBC, by ISF grant 1829/12, and by NSF grants AST-1010033, AST-1405962 and AST-1412768.

REFERENCES

- Abadi M. G., Moore B., Bower R. G., 1999, *MNRAS*, 308, 947
- Abramson A., Kenney J. D. P., 2014, *AJ*, 147, 63
- Abramson A., Kenney J. D. P., Crowl H. H., Chung A., van Gorkom J. H., Vollmer B., Schiminovich D., 2011, *AJ*, 141, 164
- Adhikari S., Dalal N., Chamberlain R. T., 2014, *J. Cosmology Astropart. Phys.*, 11, 019
- Ann H. B., Park C., Choi Y.-Y., 2008, *MNRAS*, 389, 86
- Bahé Y. M., McCarthy I. G., Crain R. A., Theuns T., 2012, *MNRAS*, 424, 1179
- Bahé Y. M., McCarthy I. G., Balogh M. L., Font A. S., 2013, *MNRAS*, 430, 3017
- Balogh M. L., Navarro J. F., Morris S. L., 2000, *ApJ*, 540, 113
- Balsara D., Livio M., O’Dea C. P., 1994, *ApJ*, 437, 83
- Bauermeister A., et al., 2013, *ApJ*, 768, 132
- Bekki K., 2009, *MNRAS*, 399, 2221
- Bekki K., Couch W. J., 2003, *ApJ*, 596, L13
- Bertschinger E., 1985, *ApJS*, 58, 39
- Bigiel F., Blitz L., 2012, *ApJ*, 756, 183
- Bigiel F., Leroy A., Walter F., Brinks E., de Blok W. J. G., Madore B., Thornley M. D., 2008, *AJ*, 136, 2846
- Binney J., Tremaine S., 2008, *Galactic Dynamics: Second Edition*, 2 edn. Princeton University Press, <http://adsabs.harvard.edu/abs/2008gady.book.....B>
- Birnboim Y., Dekel A., 2003, *MNRAS*, 345, 349
- Birnboim Y., Padnos D., Zinger E., 2016, preprint
- Bizyaev D., Mitronova S., 2002, *A&A*, 389, 795
- Blumenthal G. R., Faber S. M., Flores R., Primack J. R., 1986, *ApJ*, 301, 27
- Book L. G., Benson A. J., 2010, *ApJ*, 716, 810
- Boselli A., Gavazzi G., 2006, *PASP*, 118, 517
- Boselli A., Boissier S., Cortese L., Gil de Paz A., Seibert M., Madore B. F., Buat V., Martin D. C., 2006, *ApJ*, 651, 811
- Boselli A., Boissier S., Cortese L., Gavazzi G., 2009, *Astronomische Nachrichten*, 330, 904

- Braglia F. G., Pierini D., Biviano A., Böhringer H., 2009, *A&A*, 500, 947
- Brüggen M., De Lucia G., 2008, *MNRAS*, 383, 1336
- Bryan G. L., Norman M. L., 1998, *ApJ*, 495, 80
- Bullock J. S., Kolatt T. S., Sigad Y., Somerville R. S., Kravtsov A. V., Klypin A. A., Primack J. R., Dekel A., 2001a, *MNRAS*, 321, 559
- Bullock J. S., Dekel A., Kolatt T. S., Kravtsov A. V., Klypin A. A., Porciani C., Primack J. R., 2001b, *ApJ*, 555, 240
- Butcher H., Oemler Jr. A., 1978, *ApJ*, 226, 559
- Cayatte V., Kotanyi C., Balkowski C., van Gorkom J. H., 1994, *AJ*, 107, 1003
- Cen R., 2014, *ApJ*, 781, 38
- Close J. L., Pittard J. M., Hartquist T. W., Falle S. A. E. G., 2013, *MNRAS*, 436, 3021
- Cowie L. L., Songaila A., 1977, *Nature*, 266, 501
- Dalcanton J. J., Spergel D. N., Summers F. J., 1997, *ApJ*, 482, 659
- Danovich M., Dekel A., Hahn O., Ceverino D., Primack J., 2015, *MNRAS*, 449, 2087
- Dekel A., Birnboim Y., 2006, *MNRAS*, 368, 2
- Dekel A., Mandelker N., 2014, *MNRAS*, 444, 2071
- Dekel A., Devor J., Hetzroni G., 2003, *MNRAS*, 341, 326
- Dekel A., Sari R., Ceverino D., 2009, *ApJ*, 703, 785
- Dekel A., Zolotov A., Tweed D., Cacciato M., Ceverino D., Primack J. R., 2013, *MNRAS*, 435, 999
- Diemer B., Kravtsov A. V., 2014, *ApJ*, 789, 1
- Dressler A., 1980, *ApJ*, 236, 351
- Ebeling H., Stephenson L. N., Edge A. C., 2014, *ApJ*, 781, L40
- Ehlerst S., Werner N., Simionescu A., Allen S. W., Kenney J. D. P., Million E. T., Finoguenov A., 2013, *MNRAS*, 430, 2401
- Fang Y., Clampitt J., Dalal N., Jain B., Rozo E., Moustakas J., Rykoff E., 2016, *MNRAS*
- Ferland G. J., Korista K. T., Verner D. A., Ferguson J. W., Kingdon J. B., Verner E. M., 1998, *PASP*, 110, 761
- Finoguenov A., Reiprich T. H., Böhringer H., 2001, *A&A*, 368, 749
- Flores R., Primack J. R., Blumenthal G. R., Faber S. M., 1993, *ApJ*, 412, 443
- Font A. S., et al., 2008, *MNRAS*, 389, 1619
- Fujita Y., 2004, *PASJ*, 56, 29
- Furlanetto S. R., Loeb A., 2004, *ApJ*, 611, 642
- Gill S. P. D., Knebe A., Gibson B. K., 2005, *MNRAS*, 356, 1327
- Gisler G. R., 1976, *A&A*, 51, 137
- Gunn J. E., Gott III J. R., 1972, *ApJ*, 176, 1
- Haardt F., Madau P., 1996, *ApJ*, 461, 20
- Hansen S. M., Sheldon E. S., Wechsler R. H., Koester B. P., 2009, *ApJ*, 699, 1333
- Hernquist L., 1990, *ApJ*, 356, 359
- Jáchym P., Köppen J., Palouš J., Combes F., 2009, *A&A*, 500, 693
- Jaffé Y. L., Poggianti B. M., Verheijen M. A. W., Deshev B. Z., van Gorkom J. H., 2012, *ApJ*, 756, L28
- Jaffé Y. L., Smith R., Candlish G. N., Poggianti B. M., Sheen Y.-K., Verheijen M. A. W., 2015, *MNRAS*, 448, 1715
- Jeltema T. E., Hallman E. J., Burns J. O., Motl P. M., 2008, *ApJ*, 681, 167
- Kapferer W., Kronberger T., Ferrari C., Riser T., Schindler S., 2008, *MNRAS*, 389, 1405
- Kapferer W., et al., 2009, *A&A*, 504, 719
- Kauffmann G., Li C., Heckman T. M., 2010, *MNRAS*, 409, 491
- Kawata D., Mulchaey J. S., 2008, *ApJ*, 672, L103
- Kenney J. D. P., Geha M., Jáchym P., Crowl H. H., Dague W., Chung A., van Gorkom J., Vollmer B., 2014, *ApJ*, 780, 119
- Kennicutt Jr. R. C., 1998, *ApJ*, 498, 541
- Kennicutt Jr. R. C., et al., 2007, *ApJ*, 671, 333
- Kereš D., Katz N., Weinberg D. H., Davé R., 2005, *MNRAS*, 363, 2
- Keshet U., Waxman E., Loeb A., Springel V., Hernquist L., 2003, *ApJ*, 585, 128
- Keshet U., Waxman E., Loeb A., 2004, *ApJ*, 617, 281
- Keshet U., Kushnir D., Loeb A., Waxman E., 2012
- Klypin A., Kravtsov A. V., Bullock J. S., Primack J. R., 2001, *ApJ*, 554, 903
- Komatsu E., Seljak U., 2001, *MNRAS*, 327, 1353
- Kong X., 2004, *A&A*, 425, 417
- Kravtsov A. V., 1999, Ph.d. thesis, NEW MEXICO STATE UNIVERSITY, <http://adsabs.harvard.edu/abs/1999PhDT.....25K>
- Kravtsov A. V., 2003, *ApJ*, 590, L1
- Kravtsov A. V., 2013, *ApJ*, 764, L31
- Kravtsov A. V., Vikhlinin A., Nagai D., 2006, *ApJ*, 650, 128
- Kregel M., van der Kruit P. C., Freeman K. C., 2005, *MNRAS*, 358, 503
- Kronberger T., Kapferer W., Ferrari C., Unterguggenberger S., Schindler S., 2008, *A&A*, 481, 337
- Krumholz M. R., McKee C. F., 2005, *ApJ*, 630, 250
- Krumholz M. R., McKee C. F., Tumlinson J., 2009, *ApJ*, 693, 216
- Kushnir D., Waxman E., 2010, *J. Cosmology Astropart. Phys.*, 2, 25
- Larson R. B., Tinsley B. M., Caldwell C. N., 1980, *ApJ*, 237, 692
- Lau E. T., Nagai D., Avestruz C., Nelson K., Vikhlinin A., 2015, *ApJ*, 806, 68
- Leroy A. K., Walter F., Brinks E., Bigiel F., de Blok W. J. G., Madore B., Thornley M. D., 2008, *AJ*, 136, 2782
- Loeb A., Waxman E., 2000, *Nature*, 405, 156
- Macciò A. V., Dutton A. A., van den Bosch F. C., 2008, *MNRAS*, 391, 1940
- Madore B. F., 1977, *MNRAS*, 178, 1
- Makino N., Sasaki S., Suto Y., 1998, *ApJ*, 497, 555
- Mamon G. A., Sanchis T., Salvador-Solé E., Solanes J. M., 2004, *A&A*, 414, 445
- Marcolini A., Brighenti F., D’Ercole A., 2003, *MNRAS*, 345, 1329
- Martig M., Bournaud F., Teyssier R., Dekel A., 2009, *ApJ*, 707, 250
- Martig M., et al., 2013, *MNRAS*, 432, 1914
- McCarthy I. G., Frenk C. S., Font A. S., Lacey C. G., Bower R. G., Mitchell N. L., Balogh M. L., Theuns T., 2008, *MNRAS*, 383, 593
- Mihos J. C., 2004, Clusters of Galaxies: Probes of Cosmological Structure and Galaxy Evolution, p. 277
- Mo H. J., Mao S., White S. D. M., 1998, *MNRAS*, 295, 319
- Mo H., van den Bosch F. C., White S., 2010, *Galaxy Formation and Evolution*. Cambridge University Press
- Mok A., et al., 2013, *MNRAS*, 431, 1090
- Molnar S. M., Hearn N., Haiman Z., Bryan G., Evrard A. E., Lake G., 2009, *ApJ*, 696, 1640
- Moore B., Katz N., Lake G., Dressler A., Oemler A., 1996, *Nature*, 379, 613
- Moore B., Lake G., Quinn T., Stadel J., 1999, *MNRAS*, 304, 465
- More S., Diemer B., Kravtsov A. V., 2015, *ApJ*, 810, 36
- Moster B. P., Somerville R. S., Maulbetsch C., van den Bosch F. C., Macciò A. V., Naab T., Oser L., 2010, *ApJ*, 710, 903
- Muñoz-Cuartas J. C., Macciò A. V., Gottlöber S., Dutton A. A., 2011, *MNRAS*, 411, 584
- Nagai D., Vikhlinin A., Kravtsov A. V., 2007a, *ApJ*, 655, 98
- Nagai D., Kravtsov A. V., Vikhlinin A., 2007b, *ApJ*, 668, 1
- Navarro J. F., Frenk C. S., White S. D. M., 1996, *ApJ*, 462, 563
- Navarro J. F., Frenk C. S., White S. D. M., 1997, *ApJ*, 490, 493
- Nulsen P. E. J., 1982, *MNRAS*, 198, 1007
- Oemler Jr. A., 1974, *ApJ*, 194, 1
- Park C., Hwang H. S., 2009, *ApJ*, 699, 1595
- Pflamm-Altenburg J., Kroupa P., 2009, *ApJ*, 706, 516
- Quilis V., Moore B., Bower R., 2000, *Science*, 288, 1617
- Roediger E., 2009, *Astronomische Nachrichten*, 330, 888
- Roediger E., Brüggen M., 2006, *MNRAS*, 369, 567

- Roediger E., Brüggen M., 2007, *MNRAS*, 380, 1399
- Roediger E., Brüggen M., 2008, *MNRAS*, 388, 465
- Roediger E., Hensler G., 2005, *A&A*, 433, 875
- Ruszkowski M., Brüggen M., Lee D., Shin M.-S., 2014, *ApJ*, 784, 75
- Sarazin C. L., 1988, X-ray emission from clusters of galaxies. Cambridge Astrophysics Series, Cambridge: Cambridge University Press, 1988, <http://adsabs.harvard.edu/abs/1988xrec.book.....S>
- Schmidt M., 1959, *ApJ*, 129, 243
- Schulz S., Struck C., 2001, *MNRAS*, 328, 185
- Scott T. C., et al., 2010, *MNRAS*, 403, 1175
- Shin M.-S., Ruszkowski M., 2014, *MNRAS*, 445, 1997
- Simionescu A., et al., 2013, *ApJ*, 775, 4
- Smith R., Fellhauer M., Assmann P., 2012, *MNRAS*, 420, 1990
- Solanes J. M., Sanchis T., Salvador-Solé E., Giovanelli R., Haynes M. P., 2002, *AJ*, 124, 2440
- Spitzer Jr. L., 1942, *ApJ*, 95, 329
- Sun M., Jones C., Forman W., Vikhlinin A., Donahue M., Voit M., 2007, *ApJ*, 657, 197
- Syer D., Mao S., Mo H. J., 1999, *MNRAS*, 305, 357
- Tacconi L. J., et al., 2013, *ApJ*, 768, 74
- Tal T., et al., 2014, *ApJ*, 789, 164
- Tonnesen S., Bryan G. L., 2009, *ApJ*, 694, 789
- Tonnesen S., Bryan G. L., 2012, *MNRAS*, 422, 1609
- Tonnesen S., Stone J., 2014, *ApJ*, 795, 148
- Tonnesen S., Bryan G. L., van Gorkom J. H., 2007, *ApJ*, 671, 1434
- Toomre A., 1964, *ApJ*, 139, 1217
- Trinh C. Q., Barton E. J., Bullock J. S., Cooper M. C., Zentner A. R., Wechsler R. H., 2013, *MNRAS*, 436, 635
- Verdugo M., Ziegler B. L., Gerken B., 2008, *A&A*, 486, 9
- Voit G. M., Balogh M. L., Bower R. G., Lacey C. G., Bryan G. L., 2003, *ApJ*, 593, 272
- Vollmer B., Cayatte V., Balkowski C., Duschl W. J., 2001, *ApJ*, 561, 708
- Vollmer B., Soida M., Chung A., van Gorkom J. H., Otmianowska-Mazur K., Beck R., Urbanik M., Kenney J. D. P., 2008a, *A&A*, 483, 89
- Vollmer B., Braine J., Pappalardo C., Hily-Blant P., 2008b, *A&A*, 491, 455
- Wechsler R. H., Bullock J. S., Primack J. R., Kravtsov A. V., Dekel A., 2002, *ApJ*, 568, 52
- Weinberg M. D., 2014, *MNRAS*, 438, 3007
- Weinmann S. M., van den Bosch F. C., Yang X., Mo H. J., 2006, *MNRAS*, 366, 2
- Wetzel A. R., Tinker J. L., Conroy C., 2012, *MNRAS*, 424, 232
- Wetzel A. R., Tinker J. L., Conroy C., van den Bosch F. C., 2013, *MNRAS*, 432, 336
- Wetzel A. R., Tinker J. L., Conroy C., Bosch F. C. v. d., 2014, *MNRAS*, 439, 2687
- Woo J., Dekel A., Faber S. M., Koo D. C., 2015, *MNRAS*, 448, 237
- Zinger E., Dekel A., Birnboim Y., Kravtsov A., Nagai D., 2016, *MNRAS*, 461, 412
- Zolotov A., et al., 2015, *MNRAS*, 450, 2327
- Zwicky F., 1951, *PASP*, 63, 61
- van der Kruit P. C., Searle L., 1981a, *A&A*, 95, 105
- van der Kruit P. C., Searle L., 1981b, *A&A*, 95, 116
- van der Kruit P. C., Searle L., 1982, *A&A*, 110, 61
- von der Linden A., Wild V., Kauffmann G., White S. D. M., Weinmann S., 2010, *MNRAS*, 404, 1231